CFL3D/OVERFLOW Results for DLR-F6 Wing/Body and Drag Prediction Workshop Wing

Anthony J. Sclafani,* John C. Vassberg,† and Neal A. Harrison‡
The Boeing Company, Huntington Beach, California 92647
and
Christopher L. Rumsey,§ S. Melissa Rivers,¶ and Joseph H. Morrison**
NASA Langley Research Center, Hampton, Virginia, 23681

A series of overset grids was generated in response to the Third AIAA CFD Drag Prediction Workshop (DPW-III) which preceded the 25th Applied Aerodynamics Conference in June 2006. DPW-III focused on accurate drag prediction for wing/body and wing-alone configurations. The grid series built for each configuration consists of a coarse, medium, fine, and extra-fine mesh. The medium mesh is first constructed using the current state of best practices for overset grid generation. The medium mesh is then coarsened and enhanced by applying a factor of 1.5 to each (I, J, K) dimension. The resulting set of parametrically equivalent grids increase in size by a factor of roughly 3.5 from one level to the next denser level. Computational fluid dynamics simulations were performed on the overset grids using two different Reynolds-averaged Navier–Stokes flow solvers: CFL3D and OVERFLOW. The results were postprocessed using Richardson extrapolation to approximate grid-converged values of lift, drag, pitching moment, and angle of attack at the design condition. This technique appears to work well if the solution does not contain large regions of separated flow (similar to that seen in the DLR-F6 results) and appropriate grid densities are selected. The extra-fine grid data helped to establish asymptotic grid convergence for both the OVERFLOW FX2B wing/body results and the OVERFLOW DPW-W1/W2 wing-alone results. More CFL3D data are needed to establish grid convergence trends. The medium grid was used beyond the grid convergence study by running each configuration at several angles of attack so drag polars and lift/pitching moment curves could be evaluated. The alpha sweep results are used to compare data across configurations as well as across flow solvers. With the exception of the wing/body drag polar, the two codes compare well qualitatively showing consistent incremental trends and similar wing pressure comparisons.

Nomenclature

b = wing span
C_D = 3-D drag coefficient $= \frac{\text{drag}}{q_\infty S_{\text{ref}}}$
C_f = skin-friction coefficient
C_L = lift coefficient $= \frac{\text{lift}}{q_\infty S_{\text{ref}}}$
C_M = pitching moment coefficient
C_P = pressure coefficient $= \frac{P - P_\infty}{q_\infty}$
C_{ref} = wing reference chord $\simeq$ mean aerodynamic chord
c = chord length
N = total number of grid points
R_N = Reynolds number $= \frac{\rho_\infty V_\infty C_{\text{ref}}}{\mu_\infty}$
S_{ref} = reference area
W = wing alone
X_{ref} = X coordinate of moment reference center
x = streamwise Cartesian coordinate
Y_{ref} = Y coordinate of moment reference center
y = first cell size
y^+ = wall distance $= R_N \sqrt{\frac{c_f}{2}} y$
Z_{ref} = Z coordinate of moment reference center
α = angle of attack
Δ = difference in quantity
η = fraction of wing semispan

*Aerodynamics Engineer 4, Phantom Works. Member AIAA.
†Aerodynamics Engineer 6, Technical Fellow, Phantom Works. Associate Fellow AIAA.
‡Aerodynamics Engineer 2, Phantom Works. Member AIAA.
§Senior Research Scientist, Computational Aerosciences Branch. Associate Fellow AIAA.
¶Research Scientist, Configuration Aerodynamics Branch. Member AIAA.
**Research Scientist, Computational Aerosciences Branch. Senior Member AIAA.

I. Introduction

THE drag prediction workshop (DPW) provides a forum where both users and developers of computational fluid dynamics (CFD) programs designed to solve the Reynolds-averaged Navier–Stokes (RANS) equations can discuss issues related to overall CFD methods, including topics such as turbulence modeling and grid generation. The workshop focuses the discussion by attempting to gauge how well CFD can predict aerodynamic forces and moments for a given geometry. Drag is the primary metric used to evaluate results because of the importance accurate drag prediction has within an aircraft design environment.

The first workshop (DPW-I) took place in June of 2001. The geometry chosen for DPW-I was the DLR-F4 wing/body (WB) because it represents a typical transport configuration designed to cruise at transonic speeds and test data are publicly available. The level of participation for DPW-I was to a point where a meaningful statistical analysis could be performed on its set of CFD data. The results of the analysis were somewhat discouraging, showing a large spread in fixed-C_L drag [1]. Even though the data showed a lot of room for improvement, DPW-I was considered successful because it brought together CFD developers and practitioners and focused their efforts on a common problem. Ultimately, the findings from DPW-I reminded the CFD and applied aerodynamics communities that CFD is not yet a fully matured discipline. In addition, this workshop created a sustained interest in industry-relevant drag prediction which helped steer the DPW organizing committee to a direction of increased geometry complexity for the next workshop. For more information on DPW-I, see [2,3].

The second workshop (DPW-II) was held in June of 2003. For this workshop, the DLR-F6 was chosen as the test case geometry for the same reasons as the F4. The F6 has nearly the same WB geometry as the F4 and experimental data are available to the public. Furthermore, the F6 was tested in a wing/body/nacelle/pylon configuration. One objective of DPW-II was nacelle/pylon incremental drag prediction. At the conclusion of the second workshop, it was clear that separated flow regions at the wing/body and wing/pylon junctures made it difficult to draw meaningful conclusions with respect to grid convergence and drag prediction. As a result, the organizing committee decided to take a step back in geometry complexity for the next workshop. For more information on DPW-II, see [4,5].

The third workshop (DPW-III) was held in June of 2006. The F6 WB from DPW-II was reused as the baseline configuration for DPW-III creating a bridge between the two workshops. The primary goal of DPW-III was to revisit the WB grid convergence study with and without separated flow at the wing/body juncture. To meet this goal, a fairing was designed to eliminate the separation. Details of the fairing design can be found in [6]. The workshop committee also hoped to reduce or eliminate the wing trailing-edge separation observed in wind-tunnel flow visualization images by increasing the Reynolds number for the test case. The changes in both geometry and flow condition made DPW-III a blind test of CFD methods because no test data were available before the workshop. In addition to the F6 WB configuration, wing-alone geometries were created so workshop participants could analyze a simple configuration with no separation issues. The wing-alone test case also provided an opportunity to perform an extended grid convergence study where solutions from coarse, medium, fine, and extra-fine meshes could be evaluated.

This paper summarizes DPW-III results by comparing data from two different flow solvers (CFL3D and OVERFLOW) run on the same overset mesh. Given the higher R_N flow condition and new geometry, minimal CFD-to-tunnel data comparisons will be made. For a comprehensive OVERFLOW-to-tunnel comparison of F6 WB data at 3×10^6 R_N, see [7]. The focus of this paper will be on the results of the grid convergence study and how well the two flow solvers compare. The WB fairing and wing-alone geometries will be discussed in Sec. II, followed by some notes on grid generation in Sec. III. A complete review of the results is given in Sec. IV.

II. Geometry Descriptions

A. DLR-F6 Wing/Body and FX2B Fairing

The baseline WB configuration for DPW-III was the DLR-F6, which is the same geometry used as the test case in DPW-II. The F6 wind-tunnel model represents an aircraft designed to cruise at transonic speeds with a wing leading-edge sweep of 27.1 deg and a quarter-chord sweep of 25 deg. The dihedral of the wing is 4.787 deg. More reference quantities for this model are as follows:

$$S_{ref}/2 \qquad 72,700.0 \text{ mm}^2$$

$$C_{ref} \qquad 141.2 \text{ mm}$$

$$b/2 \qquad 585.647 \text{ mm}$$

$$AR \qquad 9.5 (\simeq 9.436)$$

$$X_{ref} \qquad 157.9 \text{ mm}$$

$$Y_{ref} \qquad 0.0 \text{ mm}$$

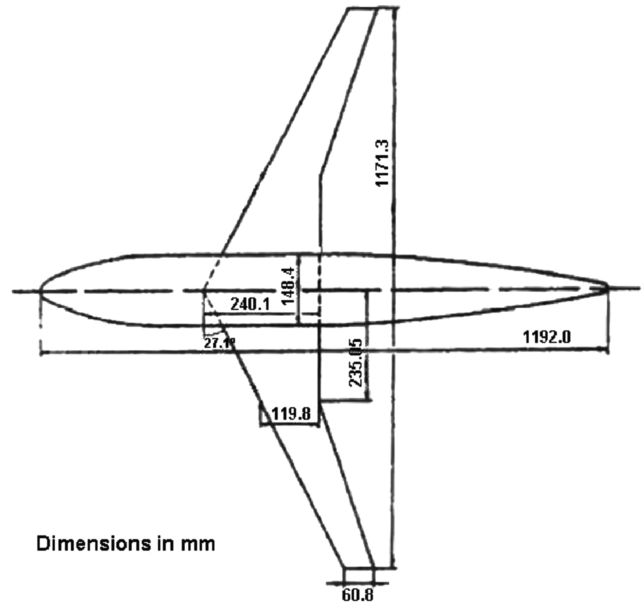$$Z_{ref} \qquad -33.92 \text{ mm}$$
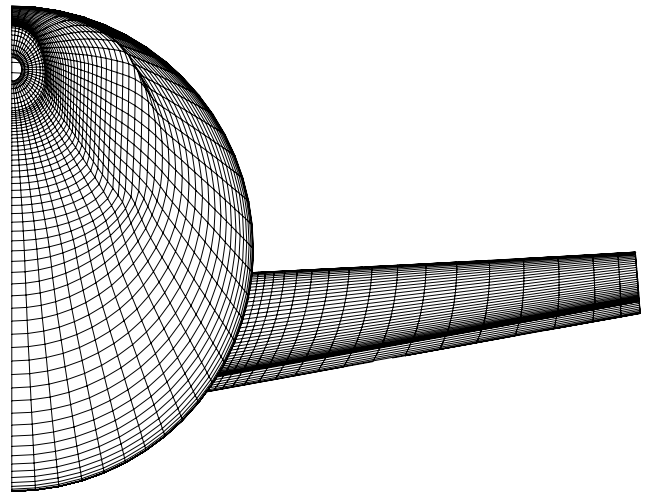

Fig. 1 DLR-F6 wing/body planform.

Fig. 2 Rear view of baseline DLR-F6 fuselage and wing root.

Note that an aspect ratio of 9.5 is used herein instead of the computed value. The purpose of this is to remain consistent with the open literature on this geometry. A planform view of the F6 WB configuration is shown in Fig. 1. For more detailed information on this geometry, see [4,8].

The DLR-F6 model has an acute angle between the fuselage and wing upper surface at the trailing edge (TE). At roughly 60 deg, this relatively low angle contributes to flow separation at the WB juncture. A view from behind the model, as shown in Fig. 2, best illustrates the problem area. To help alleviate this issue, a new WB fairing was developed by Vassberg et al. [6] with the goal of completely removing the separation bubble present at the design conditions. For consideration of a possible follow-on wind-tunnel test, the only design constraint for this fairing was that it does not cut into the baseline DLR-F6 geometry. Further, no attempt was made to optimize drag reduction. The fairing was designed in two parts. The first part represents a typical WB fairing seen on most low-wing transport aircraft. Designated FX1, this fairing is everywhere outside or tangent to the baseline fuselage and increases the fuselage-to-wing angle by about 20 deg. Figure 3 shows the rear view of FX1. To ensure fully attached WB juncture flow, a second bumplike fairing was developed. This second part to the overall fairing was designated FX2 and includes FX1 as the starting point. The FX2 fairing is shown
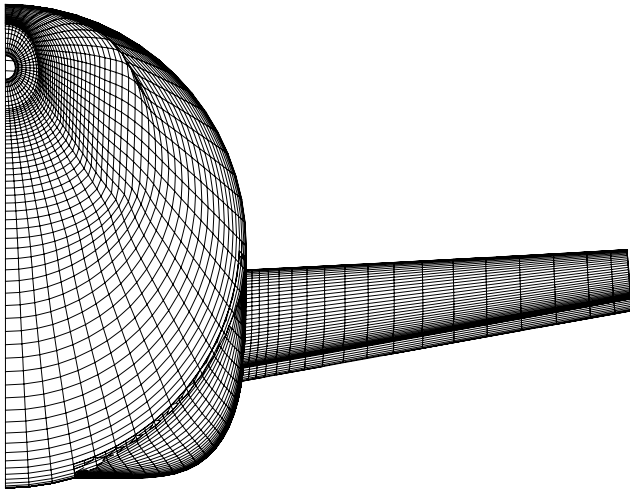
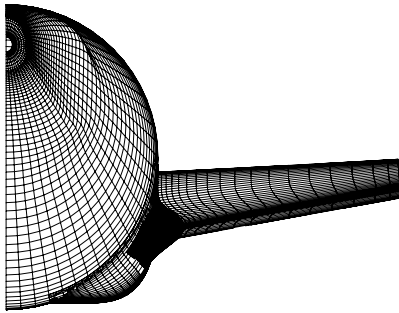**Fig. 3   Rear view of baseline DLR-F6 fuselage with FX1 WB fairing.**

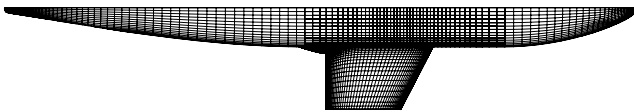**Fig. 4   Rear view of baseline DLR-F6 fuselage with FX2 WB fairing.**

Fig. 5   Top view of baseline DLR-F6 fuselage with FX2 WB fairing.

from behind the model in Fig. 4 and from above in Fig. 5. The final fairing geometry was slightly modified during the computer-aided three-dimensional interactive application (CATIA) surface generation process, hence the name FX2B.

B.   DPW Wings W1 and W2

Two wing-alone geometries (DPW-W1/W2) were developed for DPW-III. Both have in common a simple trapezoidal planform shape with no leading-edge or trailing-edge breaks. Their leading-edge sweep is 17.2 deg and they have a quarter-chord sweep of 15.0 deg. The following summarizes their reference quantities:

$S_{ref}/2$ 145,161.0mm^2 C_{ref} 197.556mm $b/2$ 762.0mm AR 8.0

W 1: X_{ref} 6847.145 mm Y_{ref} 0.0 mm Z_{ref} 2226.615 mm

W 2: X_{ref} 154.245 mm Y_{ref} 0.0 mm Z_{ref} 0.0 mm

The airfoil selected for DPW-W1 is representative of a supercritical section found on most modern transport aircraft. At the design condition of Mach 0.76 and $C_L = 0.50$, the upper-surface pressure distribution has a nearly flat, rooftop shape with a shock

located at about 57% x/c. The second wing, DPW-W2, was created by optimizing the first.

A Tranair single-point optimization at 0.76 Mach and 5×10^6 Reynolds number was performed on the DPW-W1 wing to create a test for drag increment prediction. Because the goal was to preserve the planform and thickness of the original wing, only camber and twist variables were allowed. The variables were laid out at seven spanwise cuts, with five camber and one twist variable on each cut, for a total of 42 geometry degrees of freedom. The twist variable rotates the airfoil about its trailing edge in a plane orthogonal to the y axis. In addition, the angle of attack was allowed to vary in order to maintain the same lift coefficient as the original wing.

No attempt was made to tune the locations of the geometry variables, so the camber locations were at every 0.2 in x/c, starting at 0.1, and ending at 0.9 x/c. These camber "bumps" are given by quintic B-splines which interpolate the amplitude of the central knot and vanish at neighboring endpoint knot locations. The span cuts were at 0.0, 0.2, 0.4, 0.6, 0.75, 0.90, and 1.0 in fractions of semispan. This allows the entire wing to change shape, including both the wing root and the wing tip. To prevent a singular problem definition, the twist variable at the wing root was fixed at 0. All variables express a delta change in geometry location from the initial wing.

The optimization used the variables described above to minimize the drag as computed by the far-field formulation of induced, profile, and wave drags. This was subject to the fixed lift constraint and a set of transpiration modeling constraints which are necessary to keep the optimization step size within the domain of applicability of the model problem. The optimizer used was the sequential quadratic programming algorithm, NPSOL. The largest camber change was approximately 1.4 mm in full scale units, with the twist change being between ±0.5 deg.

Additional information regarding the design of these wings is provided by Zickhur and Tinoco [9] in the workshop presentations on geometry review.

III.   Overset Grid Generation

The overset grids for the DLR-F6 wing/body and DPW-W1/W2 wing were built by the Boeing authors. As with previous workshops, the medium grid was first generated using tools and techniques that are in-line with the current state of best practices for overset grid generation [10,11]. The medium grid, which is considered typical for drag-quality design studies, was then modified by removing points for the coarser grid and adding points for the finer grid. Each grid index increased by a factor of 1.5 from one grid size to the next. In all, four grid families were constructed with each family consisting of a coarse, medium, fine, and extra-fine grid. Two grid families belong to the wing/body study and two belong to the wing-alone study. An attempt was made to construct the grids in a way that maintains surface breaks through at least three multigrid levels.

A.   DLR-F6 Wing/Body Grid

The overset grid generation process typically begins with the extraction of points from trimmed surfaces followed by surface grid generation. Because the DPW-II F6 WB geometry was carried over to DPW-III, these first two steps were already completed. The baseline F6 medium surface grid from DPW-II was the starting point for the WB grid generation process. It consisted of 12 zones—nine surface abutting grids and three box grids. Figure 6 shows the WB surface grid layout with the wing modeled by three c-mesh grids, two trailing-edge cap grids, and a wing tip cap grid. The body also has cap grids at the nose and tail.

The volume grids were regenerated to ensure adequate grid point number and spacing in the boundary layer for the higher Reynolds number flow specified for DPW-III. References [12–14] represent some of the tools used to build up the volume grids. Some basic grid information for the baseline F6 WB grid family is provided in Table 1.

Following the gridding guidelines provided by the DPW-III committee, the minimum y^+ spacing for the coarse grid was set
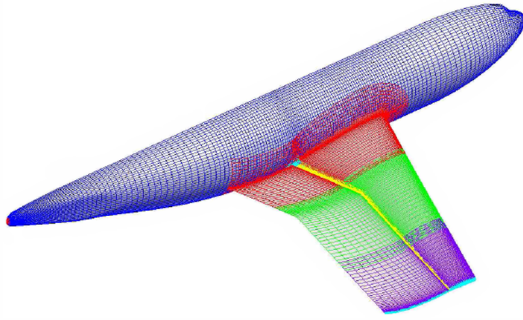
Fig. 6   DLR-F6 WB overset surface grids.

below 1.0 and the total grid size grew by a factor of roughly 3 from one grid level to the next. The number of constantly spaced cells at the surface was two for the coarse grid and increased with grid size. Views of the volume grids are provided in Figs. 7–11. Figures 7 and 8 show details of the nose and tail patches used to avoid grid singularities in the body grid. Figure 9 shows the surface abutting volume grids of the wing and body as well as the midfield box grids. Finally, Figs. 10 and 11 provide details of the wing tip and wing trailing-edge cap grids.

The FX2B medium grid was constructed by modifying some of the baseline F6 grids. The body, wing/body collar, and wing trailing-edge cap grids were updated to accurately model the FX2B fairing. More surface points were needed to capture the fairing's highly nonlinear bump shape which is characterized by a small radius in the crown-to-keel direction (see Fig. 4). This increase in surface grid points can be seen in the total grid point count summarized in Table 2.

The same process was used to build up both baseline and FX2B volume grids, so the grid parameters summarized in Tables 1 and 2 are the same except for the number of points.

B.   DPW-W1/W2 Wing-Alone Grid

The definition of the wing-alone geometry was provided as a mathematical model, so the complete grid generation process as described in [10] was employed. The surface grid layout is shown in Fig. 12. For this simple wing-alone configuration, the surface is represented by three overset grids: a c-mesh for the wing (blue, online only), a wrap-around trailing-edge cap grid (green, online only), and another wrap-around grid for the wing tip (red, online only). These three surface abutting grids are combined with two box grids to make up the overall grid system. Parameters for the complete grid family of W1 and W2 are provided in Table 3.

Figure 13 shows the volume grid layout which is similar to the wing/body grid with a single surface abutting volume grid for the wing (green, online only) and a wing tip cap grid (red, online only). The midfield box grid is also shown in this image.

IV.   Results

DPW-III participants were required to provide results on one of two test cases—the wing/body (case 1) or the wing alone (case 2). At the time of the workshop, overset structured-grid data were generated using OVERFLOW for both test cases and CFL3D for case 1. In an attempt to expand the overset database, additional CFL3D runs were made on case 2 grids. All CFL3D data presented in this paper were provided by the NASA Langley Research Center (LaRC). The majority of OVERFLOW data was provided by Boeing Phantom Works in Huntington Beach, California. LaRC attempted to run
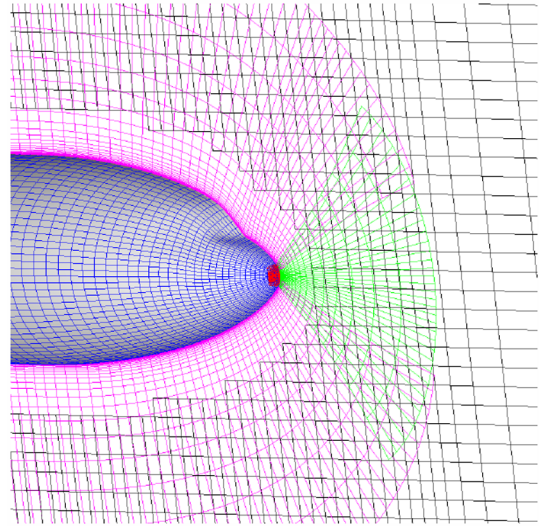

Fig. 7   DLR-F6 WB volume grid at symmetry plane: nose region.
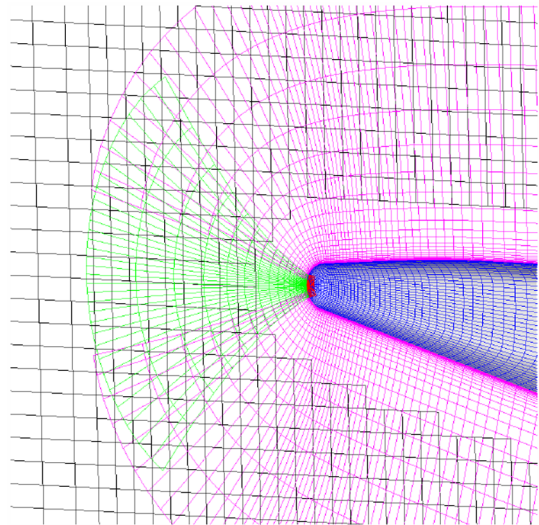

Fig. 8   DLR-F6 WB volume grid at symmetry plane: tail region.

OVERFLOW for case 1 using Menter's shear-stress-transport (SST) turbulence model, but code related problems hindered full completion of this effort. The freestream flow conditions used for both test cases are given in Table 4.

Workshop committee guidelines called for a fully turbulent boundary layer (no specified transition) and a free-air simulation, so wind-tunnel walls or the model support system were not included. The discussion of results will focus on the single-point grid convergence study for both cases. Where enough CFD data are available, CFL3D-to-OVERFLOW comparisons are made.

A.   Flow Solver and Computing Platform

Some general information on the flow solvers used to generate overset grid results will be given, and the computing platform used to run each code is briefly discussed.

Table 1   Grid information for the DLR-F6 wing/body baseline configuration

Grid	Points	First cell size	First cell y^+	Const. cells	Growth rate
Coarse	2,387,918	0.00055 mm	0.90	2	1.29
Medium	7,985,236	0.00038 mm	0.62	3	1.19
Fine	26,892,352	0.00025 mm	0.41	4	1.12
Extra fine	82,584,096	0.00019 mm	0.31	6	1.09

Fig. 9 DLR-F6 WB volume grid at wing midchord.

Fig. 11 DLR-F6 WB volume grid at wing trailing edge.
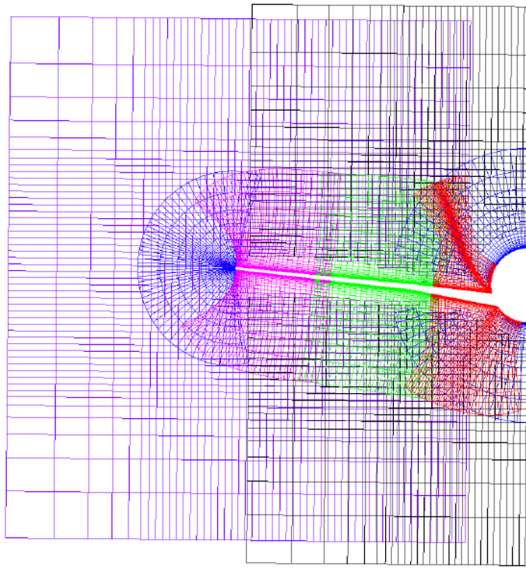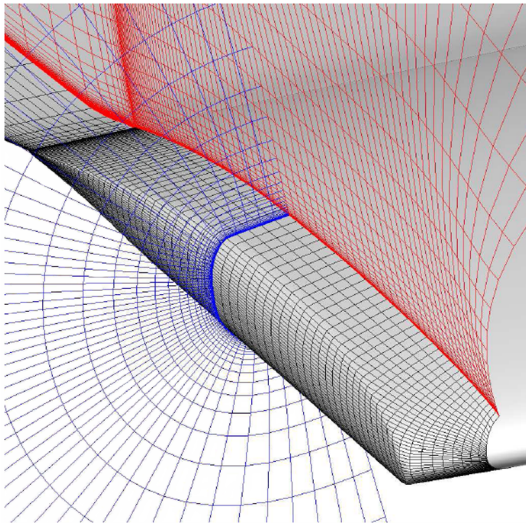
Fig. 10 DLR-F6 WB volume grid at wing tip.

Fig. 12 DPW-W1/W2 surface grid layout.

$(27 \times 10^6$ points) in full Navier–Stokes mode required 150 h of wall-clock time to complete 2000 cycles on 10 processors. Anywhere from 2000 to 5000 cycles were needed to reach full convergence, so some cases took as long as 375 h (almost 16 days) to finish. This relatively slow turnaround is partially due to the code's inability to perform mesh sequencing on overset grids and the fact that grids cannot be split for improved parallel performance. CFL3D performs significantly better on multiple block grid topologies using 1-1 blocking.

2. OVERFLOW

OVERFLOW [18] was developed by NASA with numerous contributions from academia and industry. It is a node-based RANS code specifically designed for structured overset grids. As with CFL3D, it is a general purpose 2-D/3-D solver capable of simulating steady or unsteady flows. Included in the options for turbulence modeling are the one-equation Spalart–Allmaras (SA) [19] and the two-equation Menter SST. The Boeing Phantom Works team chose

1. CFL3D

CFL3D [15,16] was developed at the NASA Langley Research Center as a cell-based RANS code for structured grids. It is a general purpose 2-D/3-D solver capable of simulating steady or unsteady flows. The boundary layer can be modeled as laminar or turbulent with a choice of several different turbulence models. The DPW-III test cases were run in both thin-layer and full Navier–Stokes modes with the upwind Roe scheme and Menter's SST [17] turbulence model.

CFL3D version 6 was run in parallel using 64-bit precision on Columbia which is a 10,240 CPU SGI Altix supercluster at the NASA Advanced Supercomputing facility. The wing/body fine grid
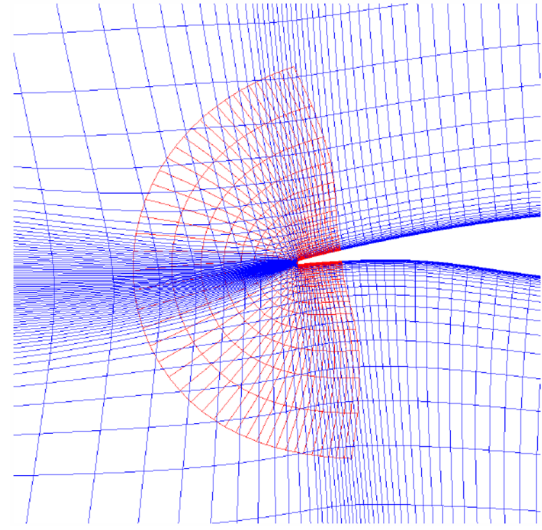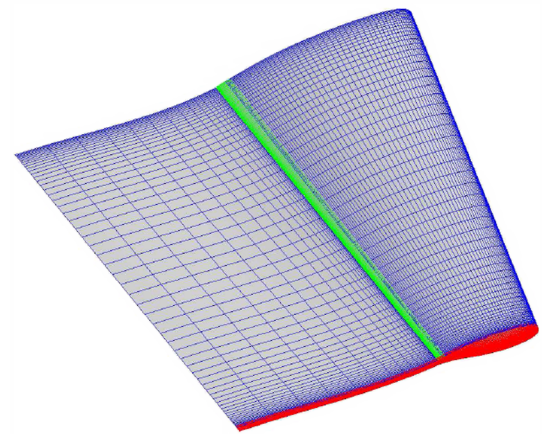
Table 2 Grid information for the DLR-F6 wing/body FX2B configuration

Grid	Points	First cell size	First cell y^+	Const. cells	Growth rate
Coarse	2,395,170	0.00055 mm	0.90	2	1.29
Medium	8,020,348	0.00038 mm	0.62	3	1.19
Fine	26,969,192	0.00025 mm	0.41	4	1.12
Extra fine	82,805,148	0.00019 mm	0.31	6	1.09

Table 3 Grid information for the DPW-W1/W2 wing-alone configuration

Grid	Points	First cell size	First cell y^+	Const. cells	Growth rate
Coarse	1,442,285	0.00055 mm	0.90	2	1.29
Medium	4,856,149	0.00038 mm	0.62	3	1.19
Fine	16,265,909	0.00025 mm	0.41	4	1.12
Extra Fine	55,014,321	0.00019 mm	0.31	6	1.09

to run OVERFLOW in a full Navier–Stokes mode with the Roe upwind scheme and SA turbulence model to be consistent with their DPW-II data [7]. A limited amount of results will be presented from thin-layer/SA and full Navier–Stokes/SST runs. The full Navier–Stokes/SST runs were made by the NASA LaRC authors.

Message Passing Interface (MPI) version 2.0z of OVERFLOW was run for this study using 64-bit precision and grid sequencing to accelerate convergence. The parallel processing was performed on a Linux PC cluster which consists of 906 Opteron dual CPU nodes with 4 GB of memory each. The wing/body fine grid (27×10^6 points) in full Navier–Stokes mode required 9 h of wall-clock time to complete 1000 cycles on 22 processors. Full convergence was achieved after 4000 cycles, so roughly 36 h were needed for each wing/body fine grid case.

B. DLR-F6 Wing/Body Results

The wing/body results are presented in four parts. The first part focuses on force and moment results from the grid convergence study. This discussion is followed by a look at wing pressures, which is intended to help explain some of the drag data trends observed in the grid study. Side-of-body and trailing-edge streamline images will also be presented in this second part. Drag polars and lift/pitching moment curves are discussed in the third part of the results section, and the fourth part addresses an OVERFLOW side study performed on the F6 medium grid.

1. DLR-F6 Grid Convergence Study

The primary objective of the grid convergence study is to approximate grid-converged values for forces and moments. In other words, this study will estimate the absolute level of drag if an infinite number of grid points are applied. Richardson extrapolation is used to evaluate the CFD data by plotting them as a function of $N^{-2/3}$, where N is the total number of points for each mesh. The $2/3$ power is based on the order of accuracy (second order) of the numerical method used to compute the results. This application of Richardson extrapolation only works if the CFD data set is from a parametrically
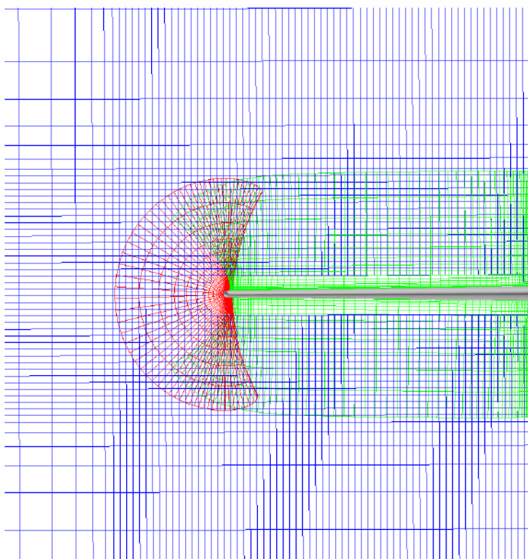
Table 4 Flow conditions

Test case	R_N (based on C_{ref})	Mach	Temperature
Wing/body	5×10^6	0.75	322.2 K
Wing alone	5×10^6	0.76	322.2 K

equivalent grid family where the coarse mesh is a subset of the next denser mesh. Salas [20] provides details on the importance of uniformly refined grids for meaningful convergence studies. If this criteria is met along with some other basic requirements such as converging all solutions to the same level and running at constant C_L for drag studies, the quality of the results can be measured by how linear they are when plotted against $N^{-2/3}$. Asymptotic grid convergence is achieved if a straight line can be drawn through the data.

For the grid convergence study, the wing/body test case was run fully turbulent at a constant C_L of 0.5. The CFL3D and OVERFLOW total drag results from the full Navier–Stokes runs are shown in Fig. 14. In this plot, baseline F6 data are colored red (online only) and FX2B data are blue (online only). The OVERFLOW-SA data include results from an extra-fine grid consisting of roughly 83×10^6 points. Because the coarse-grid drag results consistently break away from the linear trend line projected from the medium and fine grid data, an extra-fine grid is needed to help clarify whether asymptotic grid convergence is achieved. Because this extremely dense grid was built well after the workshop, CFL3D results could not be produced in time for this paper. Linear extrapolation was used to estimate the level of total drag obtained when the number of grid points goes to infinity. The arrows shown in Fig. 14 point to the extrapolated values which are summarized in Table 5.

When compared to the OVERFLOW-SA results, CFL3D-SST gives less total drag for the F6 and more for the FX2B, making the grid-converged increment between the two configurations significantly less (-9.1 counts vs -16.4 counts). The OVERFLOW-SA results show a nearly linear trend for the FX2B medium, fine, and extra-fine grid data, which is highlighted in Table 5 by the small

Fig. 13 DPW-W1/W2 volume grid at wing midchord.
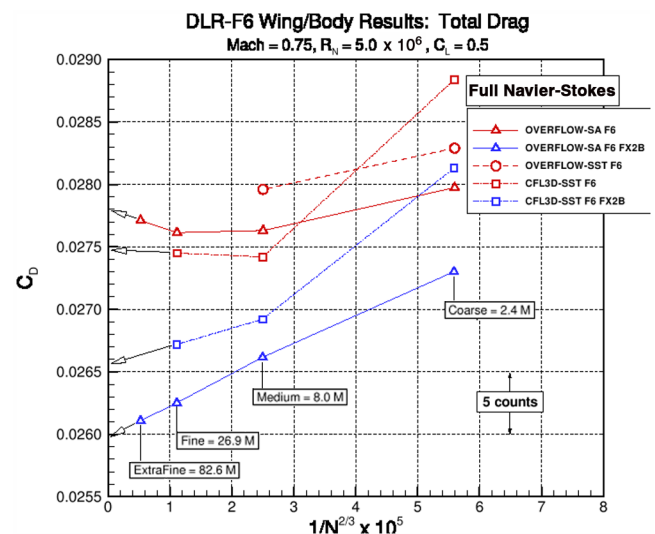
Fig. 14 DLR-F6 grid convergence study: full Navier–Stokes total drag.

Table 5   Wing/Body Total Drag Extrapolated to the Continuum, $\Delta C_D = (FX2BC_D - F6C_D)$

Source	Extrapolated grids	F6 C_D, counts	FX2B C_D, counts	ΔC_D, counts
CFL3D-SST	Medium/fine	274.7	265.6	−9.1
OVERFLOW-SA	Medium/fine	276.0	259.6	−16.4
OVERFLOW-SA	Fine/extra fine	278.0	259.8	−18.2

difference in drag between the medium/fine grid-converged value (259.6 counts) and the fine/extra-fine grid-converged value (259.8 counts). This indicates asymptotic grid convergence is essentially achieved. On the other hand, the F6 OVERFLOW-SA results do not follow a linear trend as shown in Table 5 by the 2-count difference between medium/fine and fine/extra-fine grid-converged values. Running OVERFLOW in full Navier–Stokes mode with the SA turbulence model produces results that are not in the asymptotic range of convergence for the baseline F6 configuration. This conclusion is not surprising because the F6 geometry is characterized by a large side-of-body (SOB) separation bubble. Unfortunately, the FX2B drag increment from the medium grid data is 8 counts less than the grid-converged drag increment. This large error is thought to be caused by the SOB separation present in the baseline solution. Figure 14 includes OVERFLOW-SST data for the coarse and medium F6 grids. Compared to the SA results, the SST model gives about 3.5 counts more total drag for both grids.

The full Navier–Stokes pressure and skin-friction drag components are plotted in Figs. 15 and 16, respectively. It is important to look at the drag components for the grid convergence study to rule out the possibility of canceling errors. The level of pressure drag from the various solutions, relative to each other, is similar to the total drag. In other words, the CFL3D-SST F6 fine grid pressure drag is a little lower than OVERFLOW-SA and the same can be said for the total drag. The general trends in the pressure drag data are also consistent with the total drag. The skin-friction drag data, shown in Fig. 16, are considerably less sensitive to grid refinement than pressure drag (note the tighter scale used for the skin-friction plot). The variation in OVERFLOW-SA skin friction going from coarse to extra fine is less than 0.5 counts for the F6 results and less than 2 counts for FX2B. Both codes predict higher skin friction for the FX2B configuration with a 2-count increment (FX2B-F6) for the medium grid. Finally, the F6 OVERFLOW results show the SA model computes about 1.5 counts more skin-friction drag than the SST model on the medium grid.

Pitching moment results from the full Navier–Stokes solutions are summarized in Fig. 17. Both CFL3D and OVERFLOW compute a more nose-down moment for FX2B at a C_L of 0.5. The F6 results from OVERFLOW-SA show a more linear trend than the FX2B

results which is opposite of the total drag data shown in Fig. 14. Angle-of-attack data are presented in Fig. 18. This plot shows both codes agree on the direction of the angle-of-attack change to hold C_L going from F6 to FX2B. As with drag and pitching moment, it is difficult to comment on whether or not the CFL3D results have reached asymptotic grid convergence using the coarse/medium/fine data. When the extra-fine grid data point is added to the OVERFLOW-SA results, it is easier to see that asymptotic grid convergence is achieved for angle of attack.

The NASA LaRC authors conducted a side study by running CFL3D in both thin-layer and full Navier–Stokes modes. The expression "full Navier–Stokes" means the viscous flux terms are computed in all three directions including cross terms and "thin layer" means only the terms in the viscous thin layer (i.e., boundary layer) are computed. For comparison purposes, thin-layer OVER-FLOW-SA data were generated for the medium grid only. The results are summarized in Fig. 19. F6 data are plotted in Fig. 19a and FX2B data are in Fig. 19b. The two solvers agree: a thin-layer simulation yields less drag for both configurations. Table 6 lists medium grid drag increments for the thin-layer effect.

The magnitude of the F6 drag increment is significantly larger than FX2B, once again highlighting the fundamental difference in the flowfield—the F6 SOB separation. Figure 20 compares surface streamlines on the wing upper surface at the SOB. The separation bubble is smaller in the thin-layer solution which increases the inboard wing loading allowing the angle of attack to drop for constant C_L. The angle-of-attack reduction coupled with the pressure drag reduction from a smaller separation bubble results in lower total drag. Although not shown, the CFL3D surface streamline comparison looks similar to the OVERFLOW images in Fig. 20.

The thin-layer CFL3D-SST results for the coarse, medium, and fine grids are shown in Fig. 21. The arrows point to the medium/fine grid-converged values for total drag which give an increment of −5.1 counts compared to the full Navier–Stokes grid-converged drag increment of −9.1 counts (see Table 5).

2.   DLR-F6 Wing Pressures and Streamlines

Figures 22–24 contain F6 wing pressure comparisons at semispan locations of 0.150, 0.332, and 0.637, respectively. Each figure shows
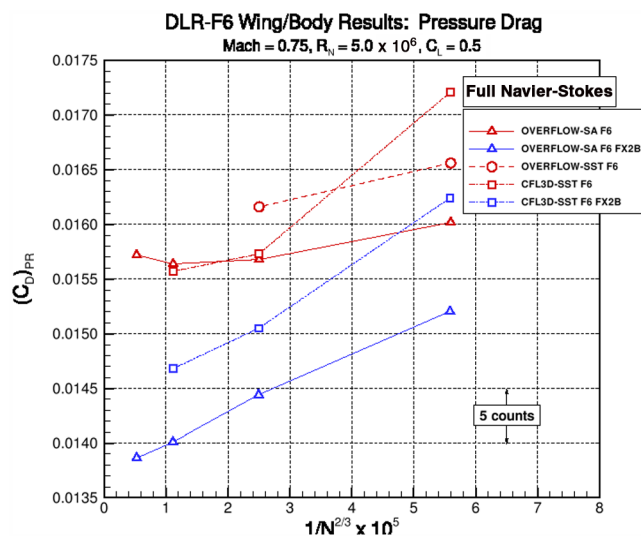
Fig. 15   DLR-F6 grid convergence study: full Navier–Stokes pressure drag.
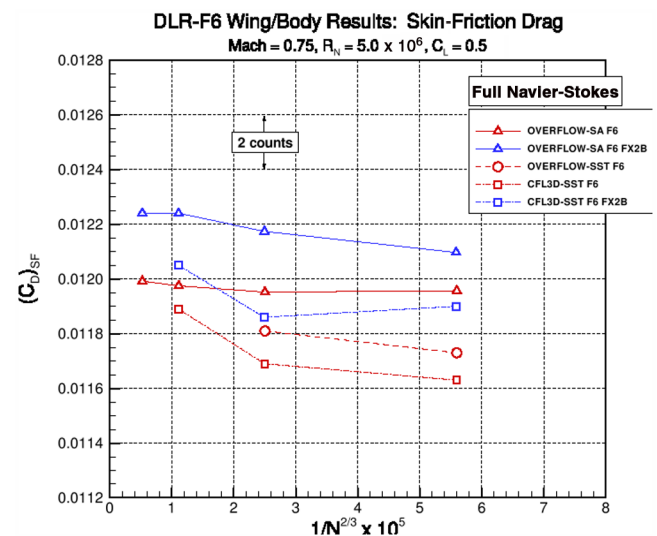
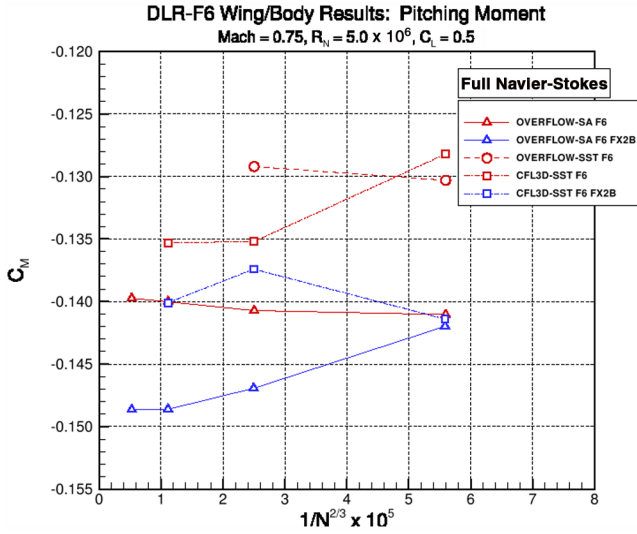Fig. 16   DLR-F6 grid convergence study: full Navier–Stokes skin-friction drag.

Fig. 17 DLR-F6 grid convergence study: full Navier–Stokes pitching moment.
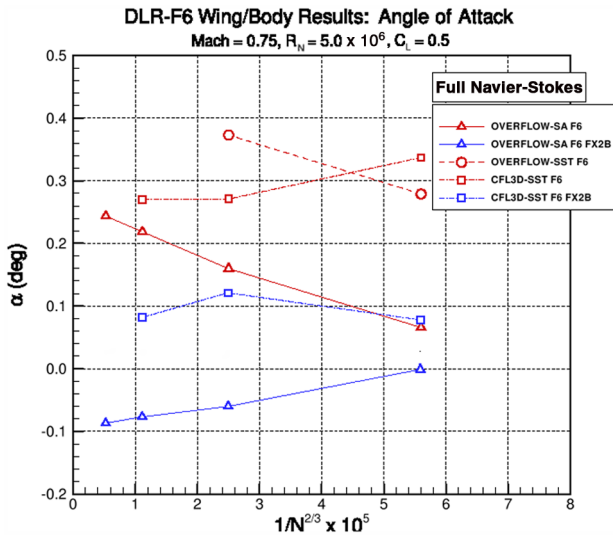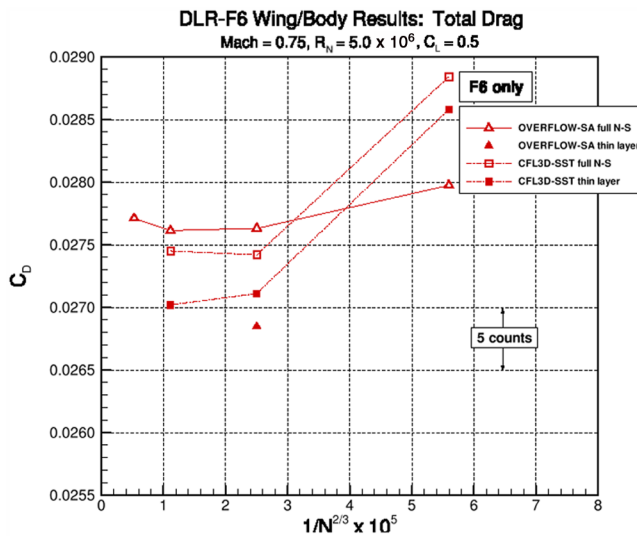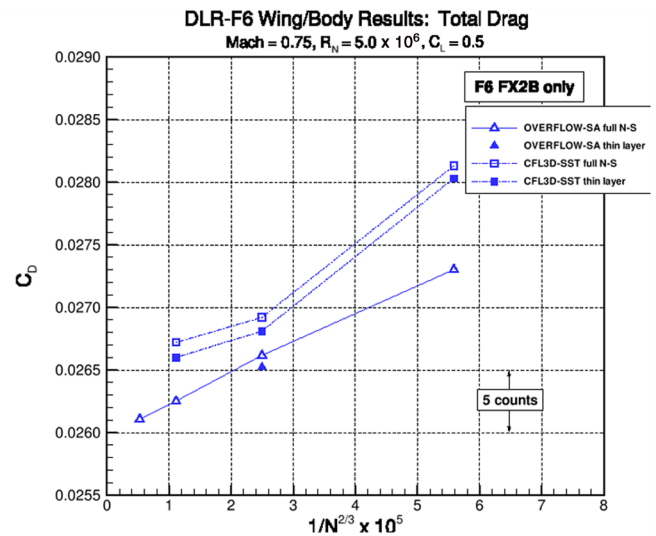

Fig. 18 DLR-F6 grid convergence study: full Navier–Stokes angle of attack.

Table 6 Thin-layer effect on medium grid drag results: $\Delta = (\text{full} - \text{thin})$

Source	F6 ΔC_D	FX2B ΔC_D
CFL3D-SST	3.1 counts	1.0 counts
OVERFLOW-SA	7.8 counts	1.1 counts

the coarse/medium/fine/extra-fine grid OVERFLOW pressures on the left and the coarse/medium/fine grid CFL3D pressures on the right. All pressures are from the grid study runs which were made at a C_L of 0.5.

The 0.150 comparison in Fig. 22 cuts through the separation bubble present on the F6 wing. This can be seen in the upper-surface pressures as recovery to freestream is not achieved. The general character of the C_p distribution is the same between codes with a minimum level of roughly -0.9 C_p occurring at about the same x/c location. Figure 23 compares pressures where the shock is strong and well defined. It is a good illustration of how grid refinement affects the computed shock location and strength. The OVERFLOW data show a significant difference in shock definition going from the coarse grid to the medium, whereas the medium/fine/extra-fine grid pressure data are tightly grouped showing minor variation in shock location. This observation helps explain why the coarse-grid drag data tend to be outside the asymptotic range of grid convergence. Although, it is unclear why the coarse-grid drag is consistently higher than the denser grids; a weaker shock will produce less wave drag. To fully understand the trend of lower drag with increasing grid points, a more detailed drag breakdown should be made. The CFL3D pressure data shown on the right of Fig. 23 give a similar story. The coarse-grid shock definition is considerably different than the medium and fine grid results. The two codes differ in that the OVERFLOW shock tends to "stand up" with grid refinement but not move very much in x/c. The CFL3D shock also stands up with grid refinement but, unlike OVERFLOW, it moves forward as well. The forward movement brings the CFL3D shock location more in-line with OVERFLOW. Both codes put the fine grid shock at about 0.24 x/c at this wing station. The pressure comparisons shown in Fig. 24 tell a similar story. The coarse-grid C_p distributions are significantly different compared to the denser grid results for both codes, and there is general agreement across solvers for the medium and fine grid pressures.

OVERFLOW surface streamlines from the medium grid solutions at a C_L of 0.5 are compared in Figs. 25 and 26. Figure 25 compares the wing/body juncture flow at the upper-surface wing trailing edge. The DLR-F6 separation bubble seen in Fig. 25a is completely
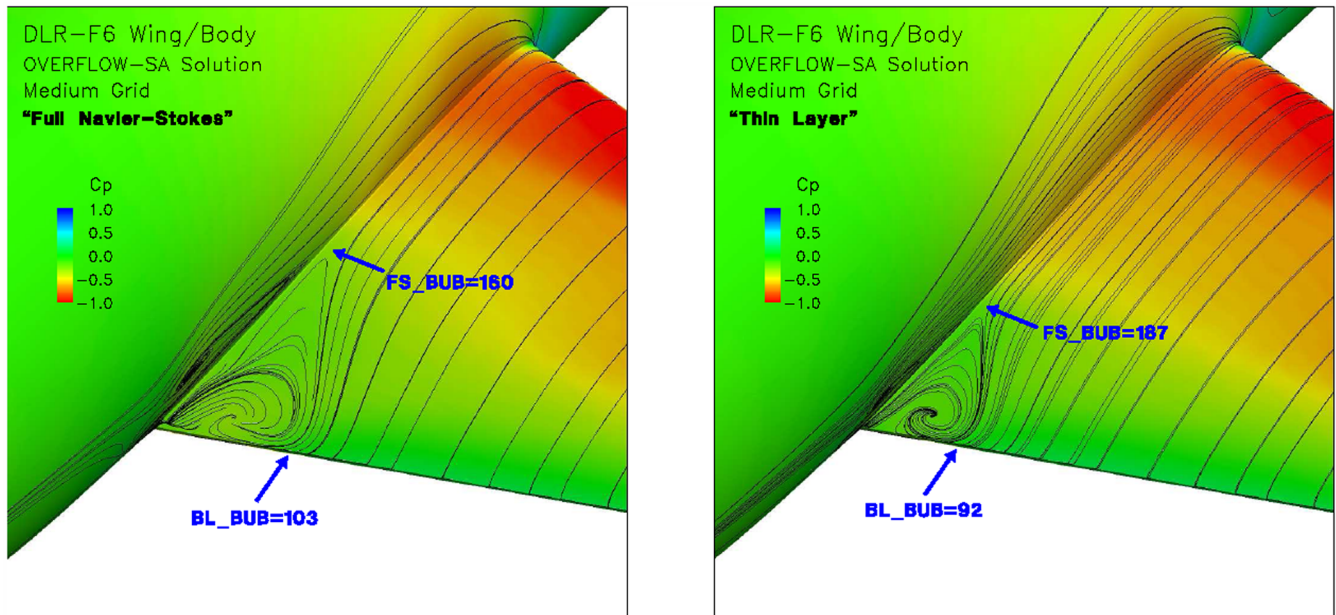

a) F6 results

b) FX2B results

Fig. 19 DLR-F6 grid convergence study: thin-layer effect.

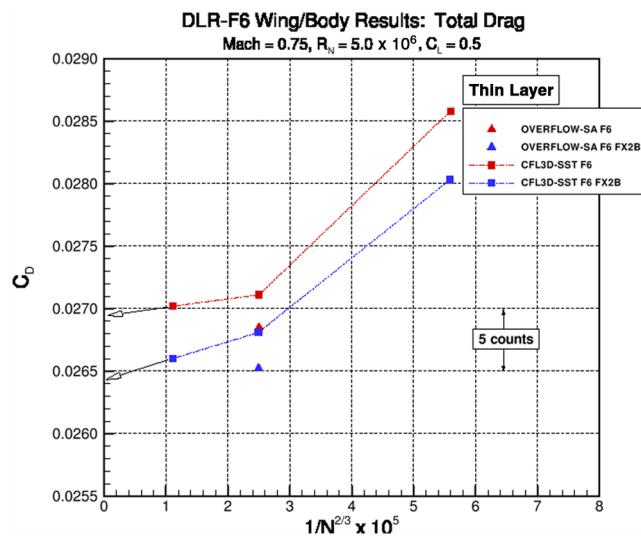**Fig. 20   DLR-F6 OVERFLOW-SA surface streamline comparison.**

Fig. 21   DLR-F6 grid convergence study: thin-layer total drag.

eliminated by the FX2B fairing as shown in Fig. 25b. The size of the separation bubble is quantified in Fig. 20 for the medium grid full Navier–Stokes solution. To see if the bubble size changes with grid refinement, the same two dimensions called out in Fig. 20 are tabulated below. The butt line (BL) coordinate is measured along the span of the wing and the fuselage station (FS) coordinate is measured along the fuselage longitudinal axis. The BL and FS coordinates for the wing trailing edge at the SOB were used to compute the length and width of the separation bubble where length corresponds to the FS direction and width to the BL direction.

The dimensions in Table 7 show the separation bubble gets larger with increasing grid density. Computed bubble size was compared against flow visualization from ONERA for DPW-II [7]. The spanwise extent (BL) of the separation bubble observed in the wind tunnel was scaled off a flow-viz image and found to be roughly 91 mm which gives a width of 27.3 mm. Every DLR-F6 medium grid OVERFLOW solution generated to date (including both DPW-II and DPW-III) computes a SOB separation bubble size larger than that observed in the ONERA test. Furthermore, running in full Navier–Stokes mode and refining the grid tends to make the bubble even larger.

Wing planform views comparing upper-surface streamlines are given in Fig. 26. These are medium grid OVERFLOW-SA solutions at a C_L of 0.5. The streamline traces show spanwise flow at the trailing edge but the boundary layer appears to be attached. For the
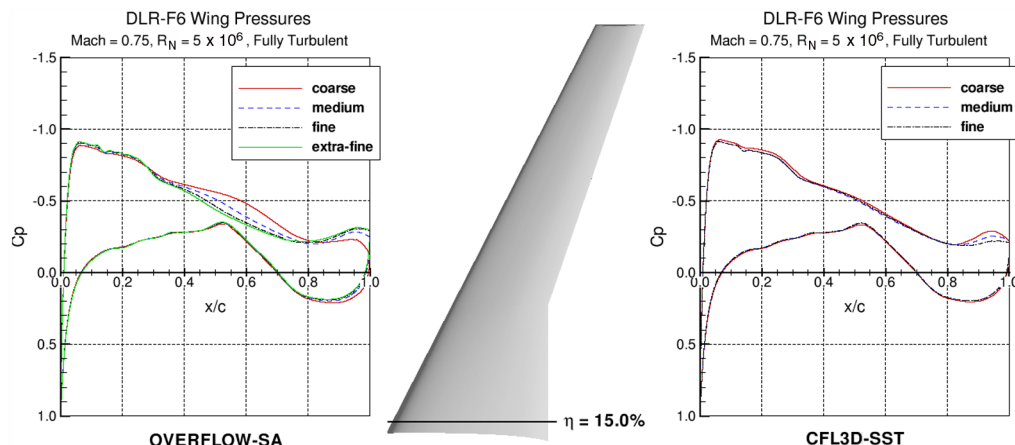

Fig. 22   DLR-F6 wing pressure comparison at 0.150 semispan.
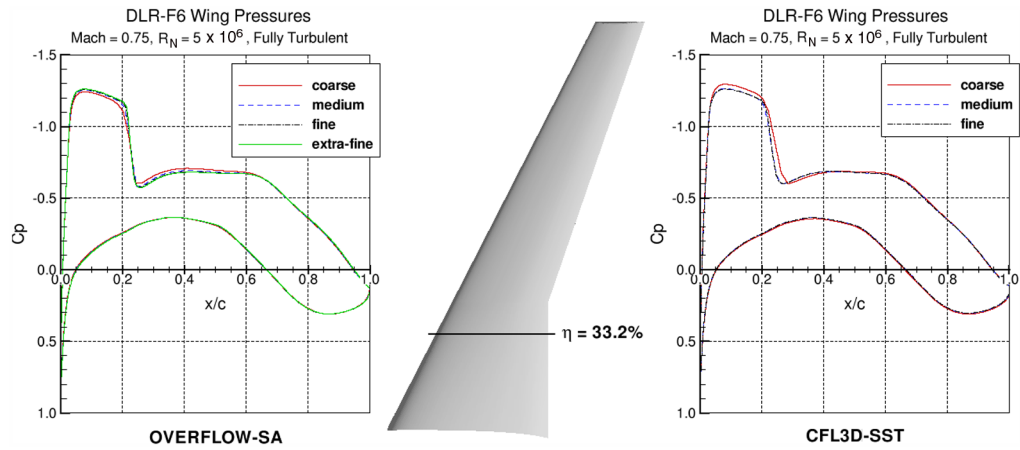
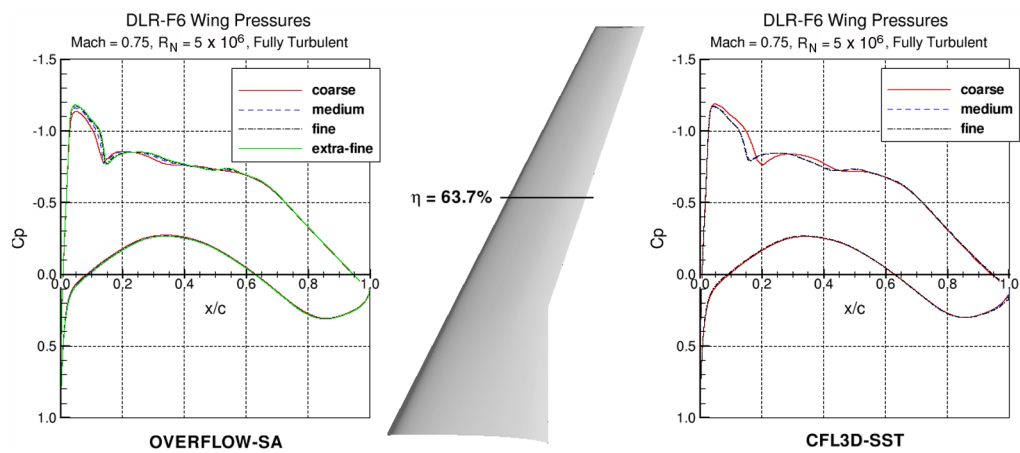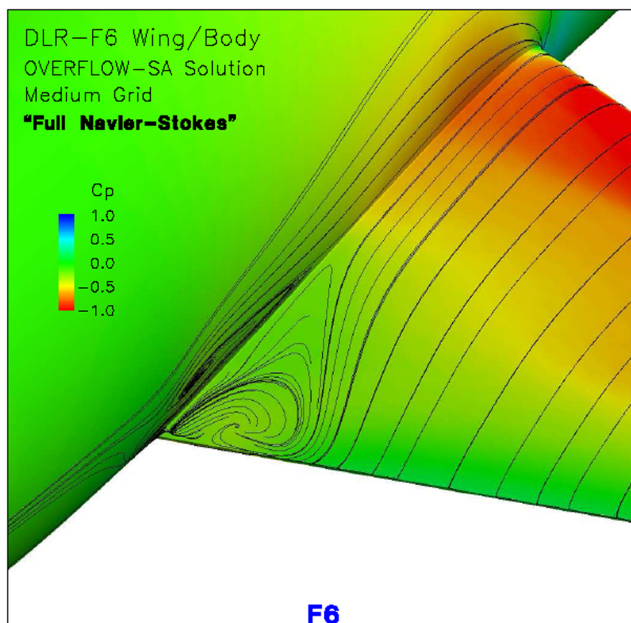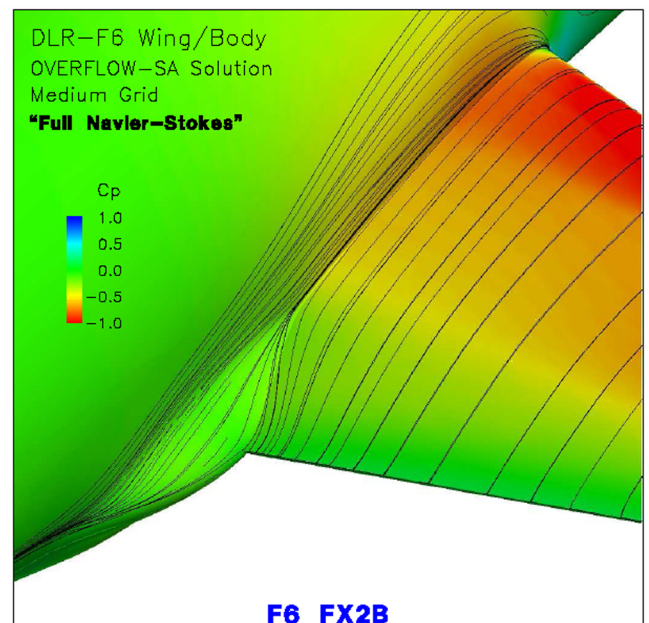Fig. 23   DLR-F6 wing pressure comparison at 0.332 semispan.

Fig. 24   DLR-F6 wing pressure comparison at 0.637 semispan.

a) F6 results

b) FX2B results

Fig. 25   DLR-F6 OVERFLOW-SA surface streamline comparison: wing/body isometric view.

Table 7   DLR-F6 OVERFLOW-SA full Navier–Stokes separation bubble size

Grid	FS, mm	BL, mm	Length, mm	Width, mm
Coarse	170.6	95.5	69.5	31.8
Medium	153.2	102.7	86.9	39.0
Fine	143.9	107.6	96.2	43.9
Extra fine	139.5	109.6	100.6	45.9

Fig. 27   DLR-F6 drag polar: baseline F6.

5×10^6 Reynolds number OVERFLOW and CFL3D solutions, no trailing-edge separation was present on either the F6 or FX2B wings for the medium and fine grids.

3.   DLR-F6 Drag Polars and Lift/Pitching Moment Curves

All data presented in this section are from full Navier–Stokes solutions where the medium grid was run at several angles of attack to establish force and moment trends.

The baseline F6 drag polar is shown in Fig. 27. This plot compares OVERFLOW results using two different turbulence models and CFL3D/OVERFLOW results using the same turbulence model. The OVERFLOW-SST polar is a rotation of the OVERFLOW-SA polar with a couple of counts more drag at low C_Ls and roughly 7 counts more at high C_Ls. The CFL3D-SST polar is not as smooth as OVERFLOW. The two sets of SST results agree well through the mid C_Ls but there is a considerable difference at the low and high ends of the polar.

Before discussing the next set of drag polars, a couple of comments must be made regarding the FX2B data submitted to DPW-III.

1) A full set of OVERFLOW-SST data could not be obtained for the FX2B configuration due to code-related problems, so angle-of-attack sweep data will not be presented for this code/configuration combination.

2) The CFL3D FX2B angle-of-attack sweep data were found to be inconsistent with the single-point grid study data. The results presented in this section are different (and considered more correct) than what was submitted to the workshop. More information on this subject is provided in the Appendix.

FX2B drag polars are compared in Fig. 28. As with the F6 drag polar comparison, the FX2B OVERFLOW-SA results look smoother (less wavy) than CFL3D-SST.

Figure 29 provides a drag polar comparison between configurations with OVERFLOW-SA results plotted in Fig. 29a and CFL3D-SST results plotted in Fig. 29b. The OVERFLOW comparison shows a drag improvement for the FX2B configuration throughout the C_L range analyzed. The CFL3D results also show a drag improvement associated with the FX2B fairing but only through the mid-C_L range.
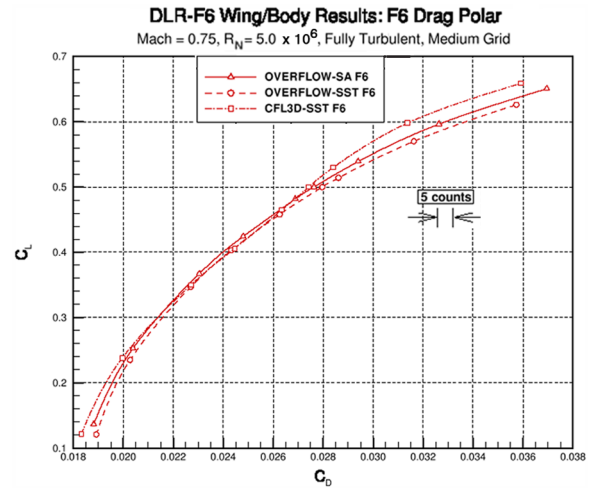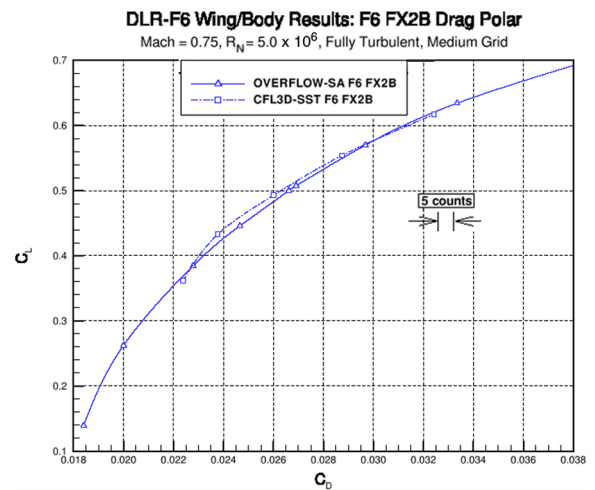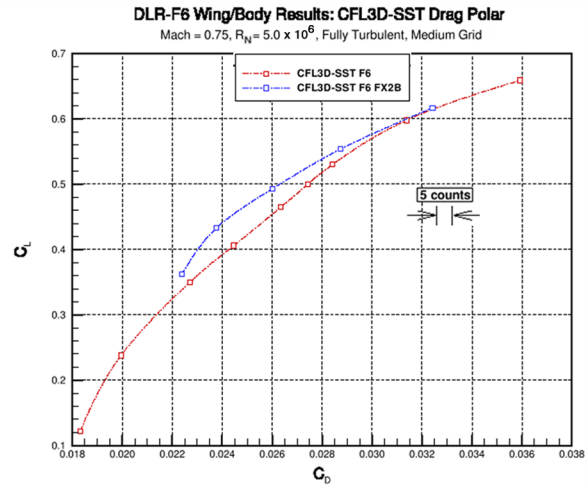

Fig. 28   DLR-F6 drag polar: F6 FX2B.

A lift curve comparison for the baseline F6 configuration is shown in Fig. 30. The OVERFLOW-SST curve is shifted to the right relative to OVERFLOW-SA. The OVERFLOW-SST simulation requires about 0.2 deg more angle of attack than OVERFLOW-SA to hold C_L. The CFL3D-SST lift curve is nearly identical to OVERFLOW-SST at angles of attack below 0 deg. Above this angle of attack, the CFL3D-SST lift curve slope increases resulting in a nonlinear trend. The FX2B lift curve comparison is given in Fig. 31.

a) F6 results

b) FX2B results
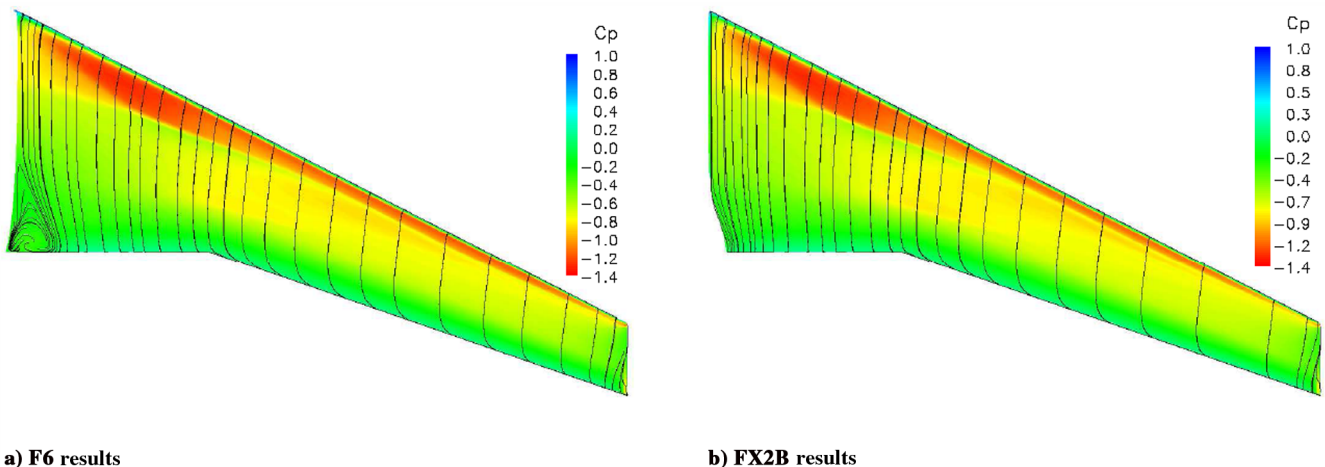
Fig. 26   DLR-F6 OVERFLOW-SA surface streamline comparison: wing planform view.
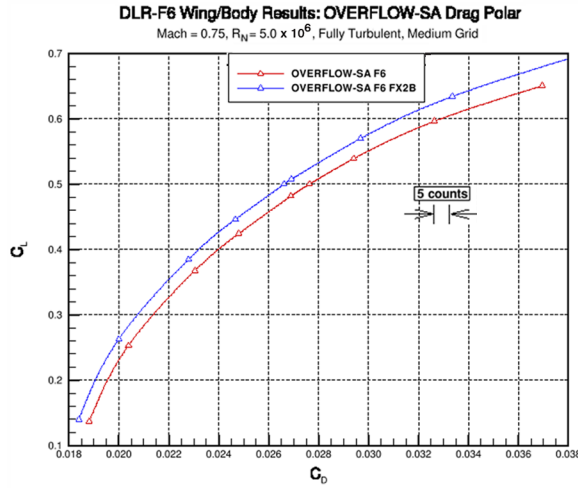
a) OVERFLOW results   b) CFL3D results

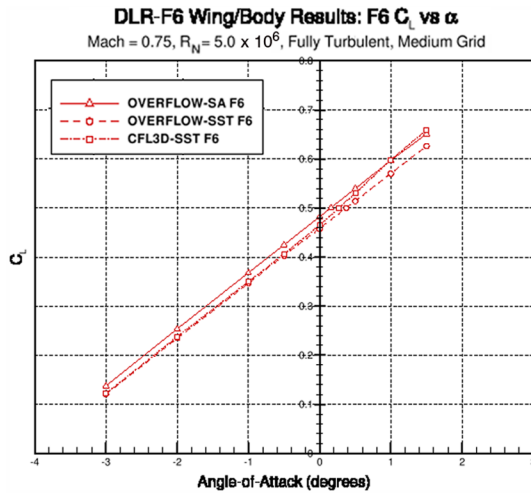Fig. 29   DLR-F6 drag polars.

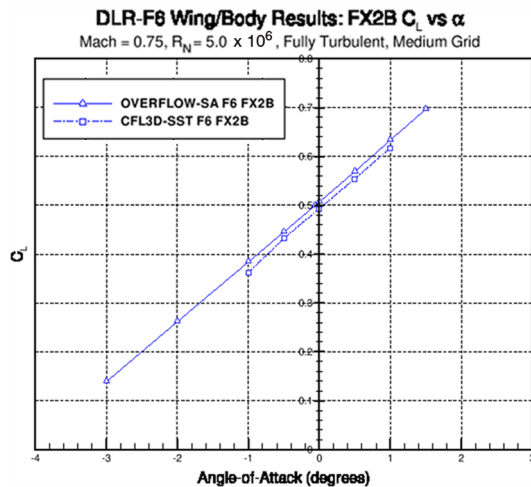Fig. 30   DLR-F6 lift curve: baseline F6.

Fig. 31   DLR-F6 lift curve: F6 FX2B.

As with the F6 data, the OVERFLOW lift curve has a more consistent slope than CFL3D at higher angles of attack.

Figure 32 compares lift curves between configurations for both OVERFLOW and CFL3D. The two codes are in general agreement.

They show very little difference between the F6 and FX2B at low angles of attack. As the angle of attack increases, FX2B produces more lift as indicated by an increase in lift curve slope relative to F6.

F6 pitching moment curves are presented in Fig. 33. All three sets of data look similar with a pitch break occurring near the design C_L of 0.5. The FX2B pitching moment comparison is given in Fig. 34 followed by the configuration comparison for OVERFLOW and CFL3D in Fig. 35. OVERFLOW shows the same C_M for both configurations at a C_L of about 0.14 while the CFL3D data meet at a higher C_L of about 0.32.

4.   DLR-F6 Trailing-Edge Grid Study

An OVERFLOW side study (motivated by a prior study by Mavriplis [21]) was performed on the baseline DLR-F6 geometry. The purpose of the study was to investigate the effect of enhancing the wing TE cap grid (see Figs. 6 and 11) in the spanwise direction only. In particular, this was done to investigate the grid effect on TE flow behavior. For DPW-II, many unstructured-grid flow solvers predicted TE separation, but most structured-grid flow solvers (including CFL3D and OVERFLOW) did not. The goal was to make the surface grid cell aspect ratio as close to 1 as possible across the trailing-edge base. This is illustrated in Fig. 36a where the enhanced inboard TE cap grid (left) is compared to the original full-wing TE cap grid (right). The image in Fig. 36b shows where these two TE cap grids meet close to the SOB. To meet the goal of a TE base cell aspect ratio (AR) of 1, the number of spanwise points on the inboard TE cap grid increased by a factor of 4.5 and the full-wing TE cap grid spanwise point count increased by a factor of 22. The wing c-mesh grids were not modified.

The TE cap grid enhancement was made on the F6 medium grid and run at the flow condition given in Table 4. The run was started from scratch at the same angle of attack as the original grid, then restarted to target the design C_L of 0.5. The results show a minimal effect. The total drag for the dense TE cap grid solution increased by 0.4 counts at a C_L of 0.5. For the same angle of attack, C_L increased by 0.004. There was no significant change to the wing/body juncture separation bubble, and no wing TE separation was observed in either the original grid or the enhanced TE cap grid solutions. This result contrasts that of Mavriplis [21] where a similar type of aspect ratio difference in two unstructured grids produced a significant decrease in lift for the same angle of attack.

C.   DPW-W1/W2 Wing-Alone Results

The wing-alone results are presented in three parts. The force and moment results from the grid convergence study are summarized in the first part. The second part is a brief look at wing pressures related to the grid study. Drag polars and lift/pitching moment curves are
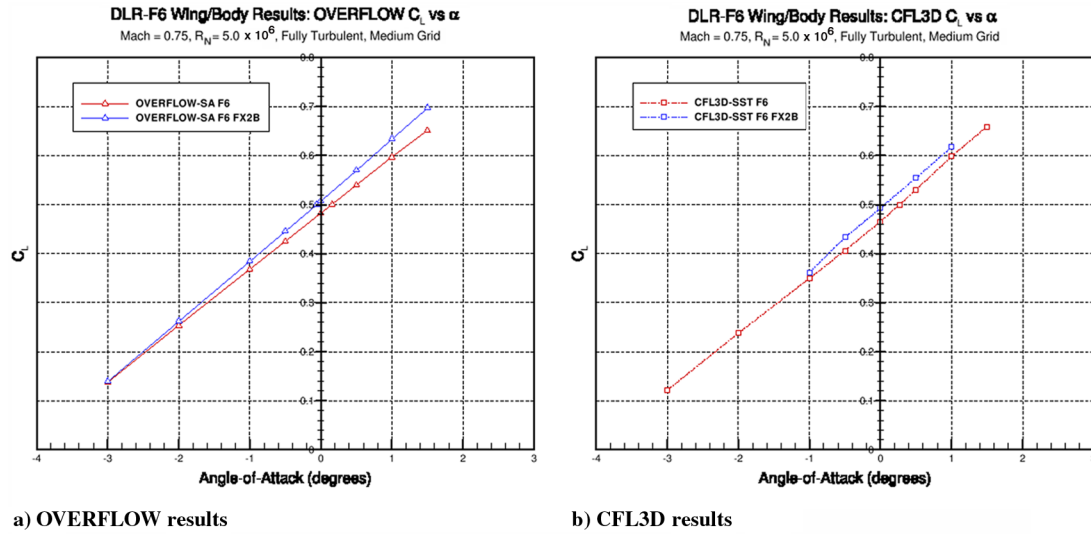
a) OVERFLOW results   b) CFL3D results

Fig. 32   DLR-F6 lift curves.

Fig. 33   DLR-F6 pitching moment: baseline F6.

Fig. 34   DLR-F6 pitching moment: F6 FX2B.

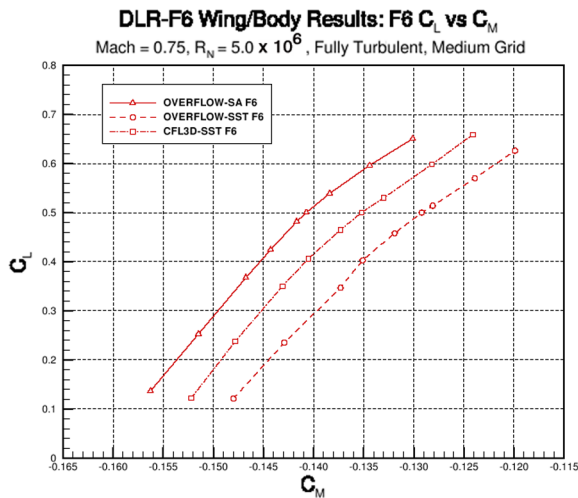discussed in the third part as well as a description of upper-surface separation development for both W1 and W2.
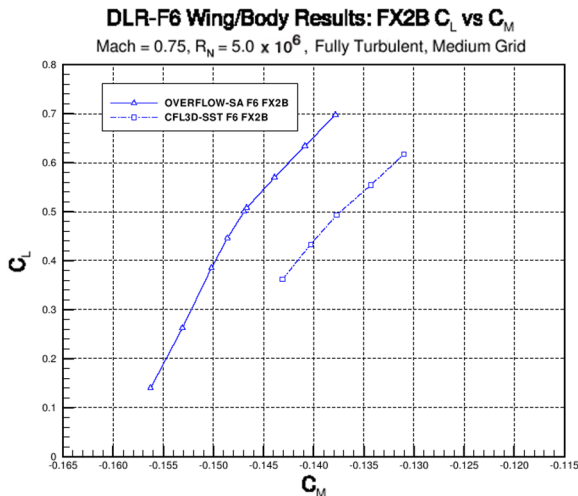
1.   DPW-W1/W2 Grid Convergence Study

Two sets of data are presented for the wing-alone grid convergence study: constant angle of attack and constant C_L. The results from the constant angle-of-attack runs made for the workshop were informative but the need for constant C_L data was apparent. After the workshop, the coarse/medium/fine/extra-fine W1 and W2 grids were run in OVERFLOW at a constant C_L of 0.5. New CFL3D results were also generated after the workshop to enhance the overset grid database. For clarity, the constant angle-of-attack and constant C_L data plots will be presented side by side when appropriate. All data presented here are from full Navier–Stokes simulations.

Total drag is plotted against grid size in Fig. 37. Note that the same scale is used on both the constant angle-of-attack plot in Fig. 37a and the constant C_L plot in Fig. 37b. When analyzed at the same angle of attack, the OVERFLOW-SA data show the optimized W2 wing has more drag than W1. The W2 wing does have a significant drag improvement at 0.5 C_L as indicated in Fig. 37b. This is a good example of why drag studies are typically performed at constant C_L conditions. The data presented in Fig. 37 suggest the extra-fine grid results help establish asymptotic grid convergence for this simple wing-alone geometry. The coarse-grid data tend to fall further away from the asymptote, particularly for the constant angle-of-attack drag trends. This behavior is consistent with the results of the wing/body grid convergence study.

Unfortunately, adequate time and resources were not available to obtain a full set of CFL3D data for the wing-alone test case. The W1 coarse/medium/fine grids were analyzed at constant angle of attack and only the W1 coarse/medium grids were analyzed at constant C_L. No CFL3D W2 cases were run. The CFL3D W1 medium/fine grid data are extrapolated to the continuum along with the OVERFLOW data at constant angle of attack. The extrapolated total drag data are summarized in Table 8.

Based on these results, CFL3D-SST predicts roughly 3 counts less drag for W1 than OVERFLOW-SA at 0.5 deg angle of attack. The results in Table 8 also show how the medium/fine/extra-fine grid data follow a nearly linear trend with grid refinement with less than a 1-count drag difference at the continuum between the medium/fine and fine/extra-fine extrapolated data. The same extrapolation is made on the constant C_L OVERFLOW-SA results plotted in Fig. 37b.

Table 9 does not include CFL3D results because the fine and extra-fine grids were not analyzed at constant C_L. Once again, asymptotic grid convergence is demonstrated in the OVERFLOW-SA results with only a 0.1-count difference in the W1 constant C_L extrapolated
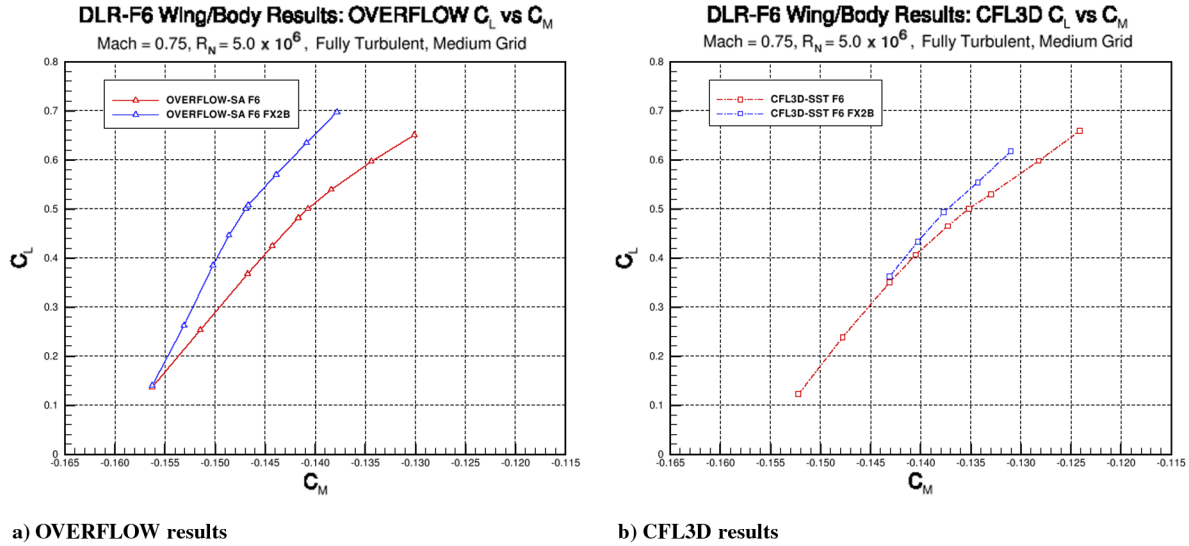
a) **OVERFLOW results**   b) **CFL3D results**

Fig. 35   DLR-F6 pitching moment.

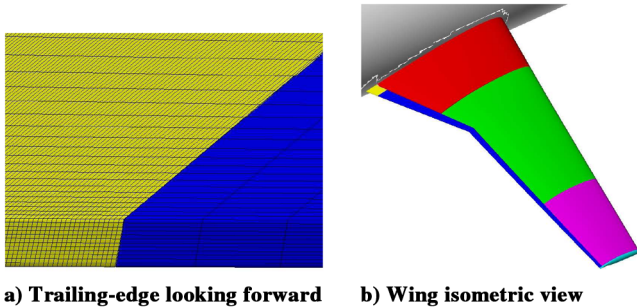a) **Trailing-edge looking forward**   b) **Wing isometric view**
Fig. 36   DLR-F6 dense trailing-edge cap grid study.

data and a 0.7-count difference in the W2 data. Using the fine/extra-fine grid extrapolated total drag levels, the wing optimization produces a 10.5-count drag improvement at a C_L of 0.5.

The grid-converged pressure drag data are presented in Fig. 38 with constant angle-of-attack results in Fig. 38a and constant C_L in Fig. 38b. In general, the pressure drag trends with grid refinement are very similar to the total drag results. This leads one to believe the

other drag component, skin friction, should be relatively insensitive to grid refinement. Figure 39 shows just that. The OVERFLOW-SA skin-friction drag results are nearly unchanged with grid convergence for both constant angle-of-attack and constant C_L runs. The CFL3D-SST W1 data at constant angle of attack do show more variation, but the skin friction increases by less than 1 count going from the medium grid to the fine grid.

Pitching moment data are presented in Fig. 40. The constant angle-of-attack OVERFLOW-SA data indicate W2 has a slight nose-up pitching moment shift relative to W1. The constant C_L data actually cross over at about the medium grid size. Considering the scale used for the pitching moment plots ($\Delta C_M = 0.001$), the medium/fine/extra-fine grid data appear to be close to the asymptotic range of grid convergence.

The lift coefficient from the constant angle-of-attack runs is plotted against grid size in Fig. 41. The OVERFLOW-SA results indicate W2 produces about 0.02 more C_L at an angle of attack of 0.5 deg, and the medium grid W1 data show CFL3D-SST predicts about 0.008 less C_L than OVERFLOW-SA. Once again, the medium/fine/extra-fine grid C_L data for both W1 and W2 are considered close to asymptotically approaching the continuum. Grid convergence results for angle of attack from the constant C_L runs are given in Fig. 42. This plot shows CFL3D and OVERFLOW agree
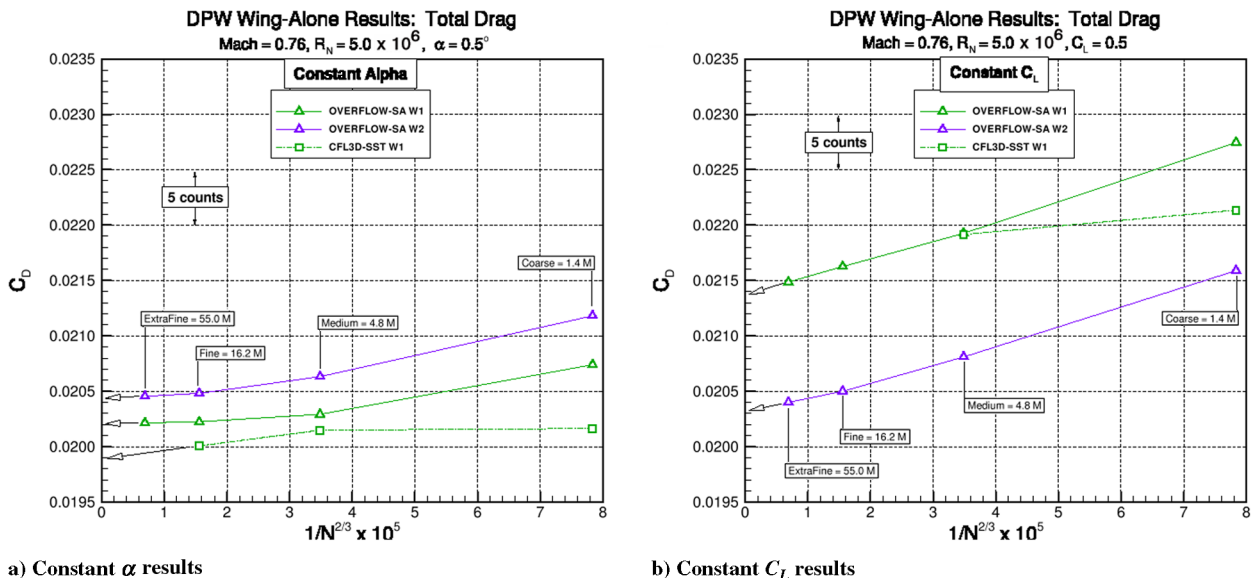

a) **Constant α results**   b) **Constant C_L results**
Fig. 37   DPW-W1/W2 grid convergence study: total drag.

Table 8 Wing-alone total drag at constant α extrapolated to the continuum

| Source	Extrapolated grids	W1 C_D, counts	W2 C_D, counts
CFL3D-SST	Medium/fine	198.9	N/A
OVERFLOW-SA	Medium/fine	201.7	203.6
OVERFLOW-SA	Fine/extra fine	202.1	204.3

Table 9 Wing-alone total drag at constant C_L extrapolated to the continuum

Source	Extrapolated grids	W1 C_D, counts	W2 C_D, counts
OVERFLOW-SA	Medium/fine	213.8	202.5
OVERFLOW-SA	Fine/extra fine	213.7	203.2

reasonably well on angle of attack for the W1 coarse and medium grids. The OVERFLOW-SA results show a nearly constant angle-of-attack increment for all grid sizes analyzed with W2 requiring roughly 0.2 deg less angle of attack to hold C_L constant at 0.5. As with all other wing-alone OVERFLOW results, the variation in angle of attack with grid refinement has a linear character.

2. DPW-W1/W2 Wing Pressures

Pressure comparisons from the W1 wing-alone test case are provided in Fig. 43. The pressures were extracted from the 0.5 C_L solutions at a midwing semispan station of $\eta = 0.551$. The OVERFLOW-SA data, shown on the left, are consistent with the wing/body C_p comparison in that the coarse-grid shock is considerably weaker than the next denser mesh. The CFL3D-SST data, shown on the right, have the same trend for shock strength but they are not nearly as dramatic as the OVERFLOW results. Because this observation is made on both test cases, it can be said with some confidence that the coarse grid does not have adequate resolution to accurately model typical transonic pressure distributions. If the wing shock strength and location is not well predicted, computing absolute
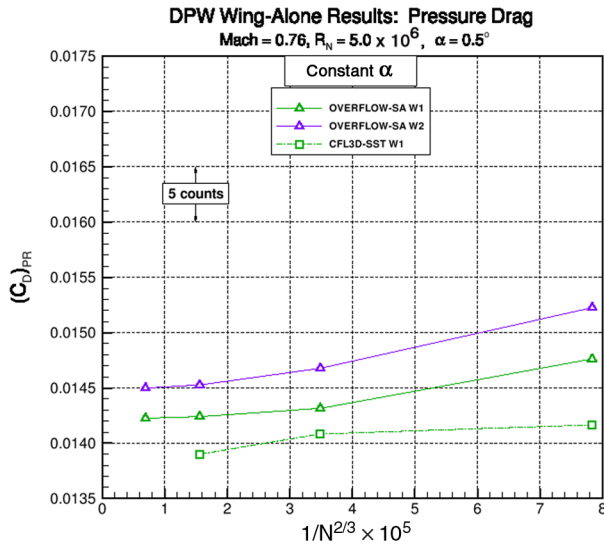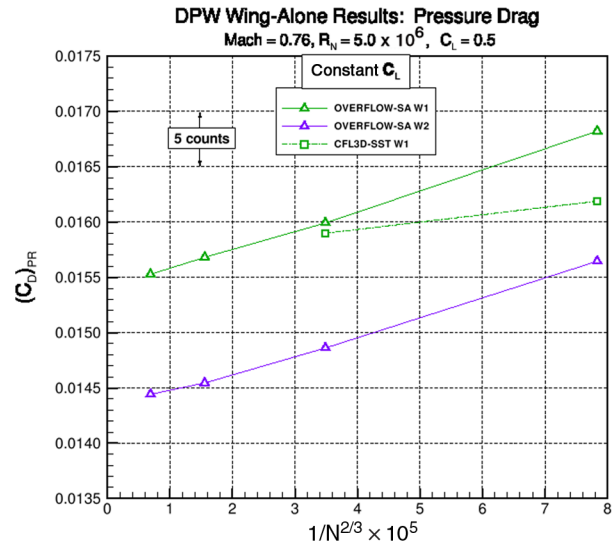
a) Constant α results   b) Constant C_L results

Fig. 38   DPW-W1/W2 grid convergence study: pressure drag.
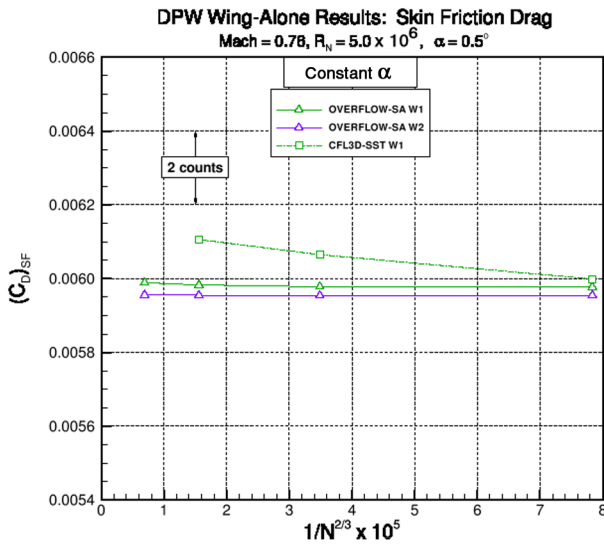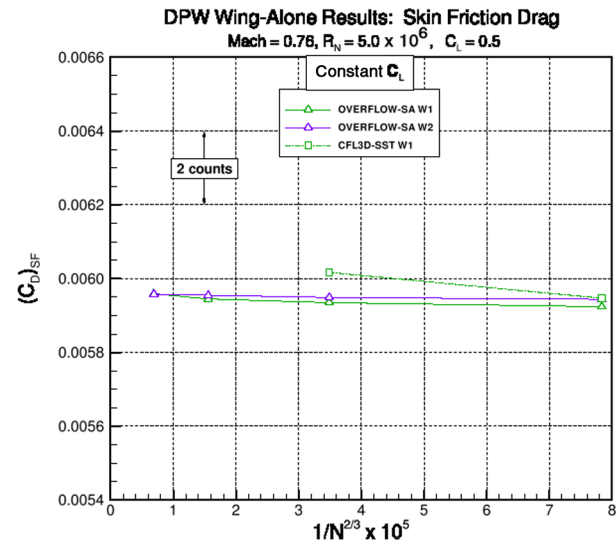
a) Constant α results   b) Constant C_L results

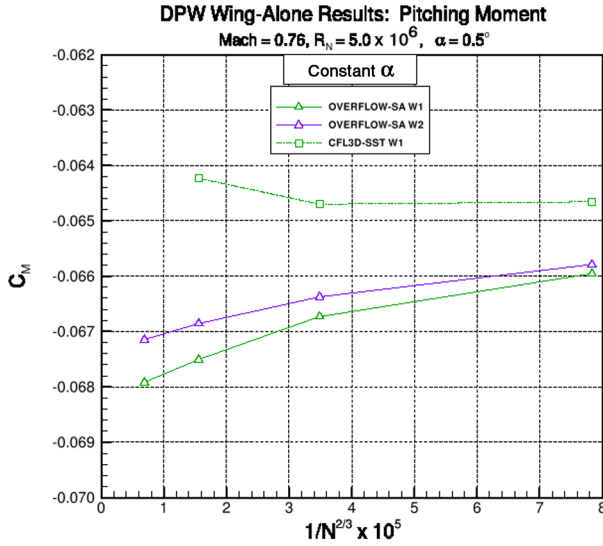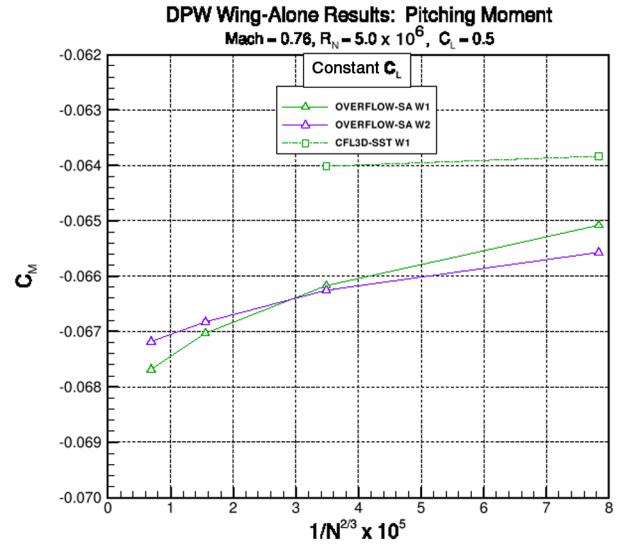**Fig. 39   DPW-W1/W2 grid convergence study: skin-friction drag.**

a) Constant α results

b) Constant C_L results

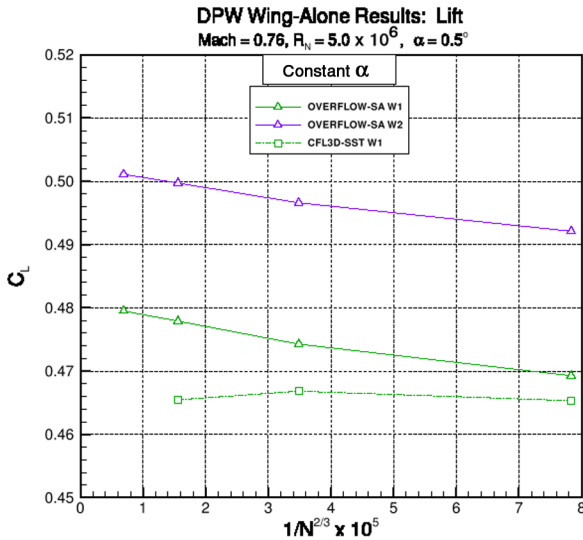Fig. 40 DPW-W1/W2 grid convergence study: pitching moment.

Fig. 41 DPW-W1/W2 grid convergence study: lift at constant angle of attack.
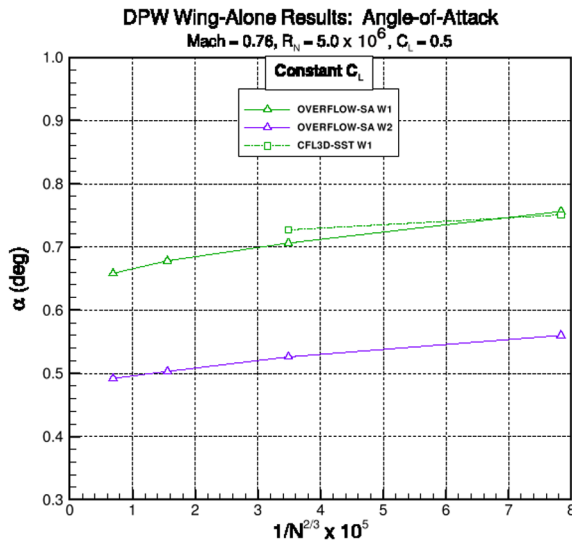

Fig. 42 DPW-W1/W2 grid convergence study: angle of attack at constant lift.

drag to an error level of a few percent becomes even more challenging.

3. DPW-W1/W2 Drag Polars, Lift/Pitching Moment Curves, and Streamlines

The medium grid drag polars are shown in Fig. 44. The W1 data (green lines/symbols) (online only) compare well between codes for the two conditions run in CFL3D. The W2 OVERFLOW-SA polar (purple line/symbols) (online only) has a different shape than the W1 polar with the two crossing over at C_Ls below and above the design point. The W2 drag improvement is roughly 11 counts at the design C_L of 0.5, but this optimized wing performs worse than W1 at the low and high ends of the polar. This is not surprising given a single-point optimization was used to generate the W2 wing (see Sec. II.B).

Lift curves for the medium grid angle-of-attack sweep runs are provided in Fig. 45. The two CFL3D-SST data points, at C_Ls of 0.47 and 0.50, are very close to the OVERFLOW-SA curve. For C_Ls up to about 0.6, the W2 wing provides the same lift as W1 with about a 0.2 deg reduction in angle of attack. At roughly 0.66 C_L, the W2 lift curve crosses over the W1 curve.

Figure 46 compares the wing-alone pitching moment curves. The CFL3D-SST data show a more nose-up moment compared to the OVERFLOW-SA curve at the same C_L. CFL3D predicts W1 gives roughly 0.002 more nose-up moment than OVERFLOW at the design point. The W1/W2 OVERFLOW comparison indicates a difference in how the flow separates across the span with angle of attack.

Figures 47–49 compare W1/W2 upper-surface streamlines at angles of attack of 0.5, 1.5, and 2.5 deg, respectively. These streamline images were generated using medium grid OVERFLOW-SA solutions. The streamlines at 0.5 deg angle of attack show attached flow for both wings. It is actually more interesting to note the difference in upper-surface pressure contours in Fig. 47. At this angle of attack, the W2 shock is clearly weaker. The next comparison is made at 1.5 deg because this is the approximate angle of attack where flow separation begins at the foot of the shock. Figure 49 shows that, at 2.5 deg, the upper-surface flow is completely separated downstream of the shock on both wings.

V. Conclusions

The DLR-F6 wing/body with and without the FX2B fairing and the DPW-W1/W2 wing-alone configurations from the third Drag Prediction Workshop were analyzed using the two widely used CFD codes, CFL3D and OVERFLOW. A parametrically equivalent set of overset grids were generated by first building a grid based on
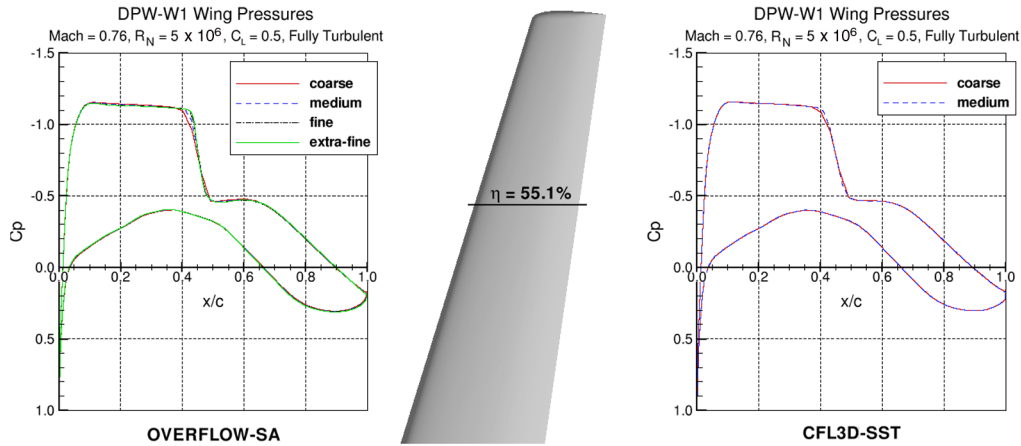
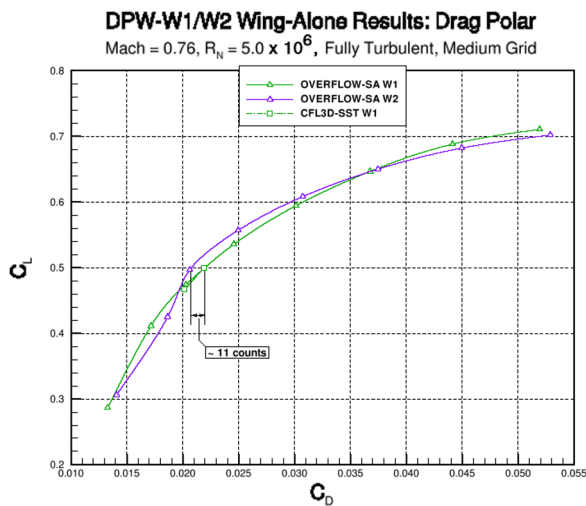**Fig. 43 DPW-W1 wing pressure comparison at 0.551 semispan.**
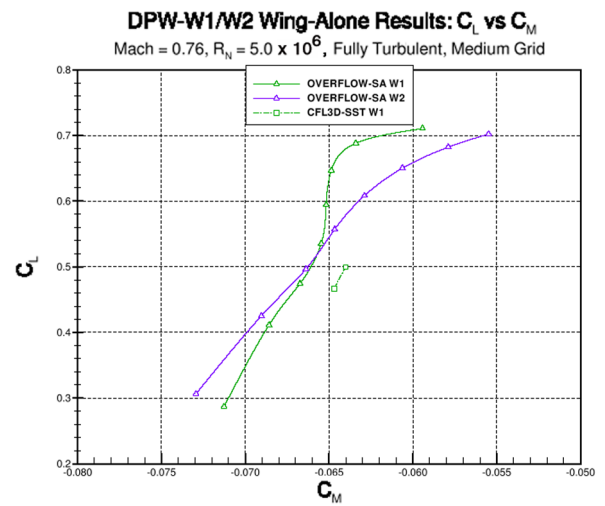

Fig. 44 DPW-W1/W2 drag polars.

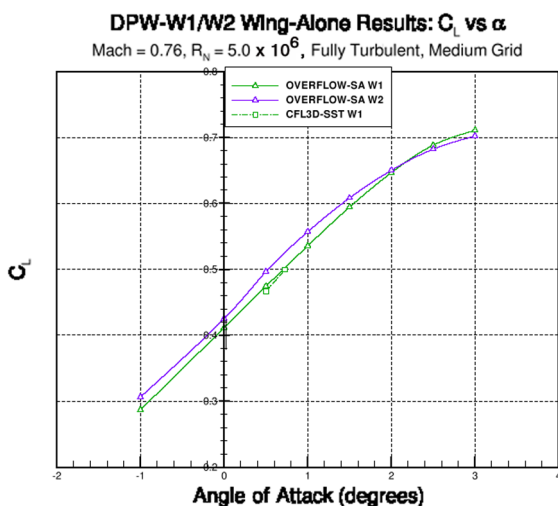**Fig. 46 DPW-W1/W2 pitching moment.**

Fig. 45 DPW-W1/W2 lift curves.

guidelines for cruise drag prediction studies. This grid, referred to as the medium-sized grid, was modified by reducing and increasing the total number of grid points by a factor of 3.5 to create the coarse and fine grids. The fine grid was then enhanced again by the same factor to produce the extra-fine grid. The CFD results from these uniformly refined grid families were postprocessed using Richardson extrapolation which, in theory, can be used to establish grid resolution requirements for accurate drag prediction. This grid convergence study showed that the low resolution coarse-grid data are insufficient for accurate drag prediction. This is due, in part, to differences in computed shock strength and location, where the coarse-grid solution stands apart from the rest for both flow solvers and configurations analyzed.

With the use of a fourth extra-fine mesh, it appears that the medium/fine/extra-fine results on the FX2B configuration fall within the asymptotic range of grid convergence. However, this is not the case with the baseline DLR-F6 geometry. Furthermore, the medium/fine/extra-fine results of both DPW-W1 and DPW-W2 wings appear to be within the asymptotic range. Based on these findings, it seems that moderately sized pockets of flow separation can be a root cause for poor grid convergence. This conclusion is somewhat in contrast to that of [22], which assessed results from a much larger community with wider variation in grid types, grid quality, and turbulence models. The conclusion herein is based on OVERFLOW results on overset meshes.

To illustrate the impact of the F6 side-of-body separation on grid convergence, the computed drags from the fine and extra-fine grids were extrapolated to the continuum to approximate grid-converged drag. Using the results of this extrapolation, the FX2B drag increment (FX2B-F6) from an infinitely refined grid was 8 counts larger than the increment computed using the medium grid results. Making the same type of comparison for the wing-alone case, the drag increment (W2-W1) from an infinitely refined grid was 0.7 counts lower than the medium grid increment. This exercise
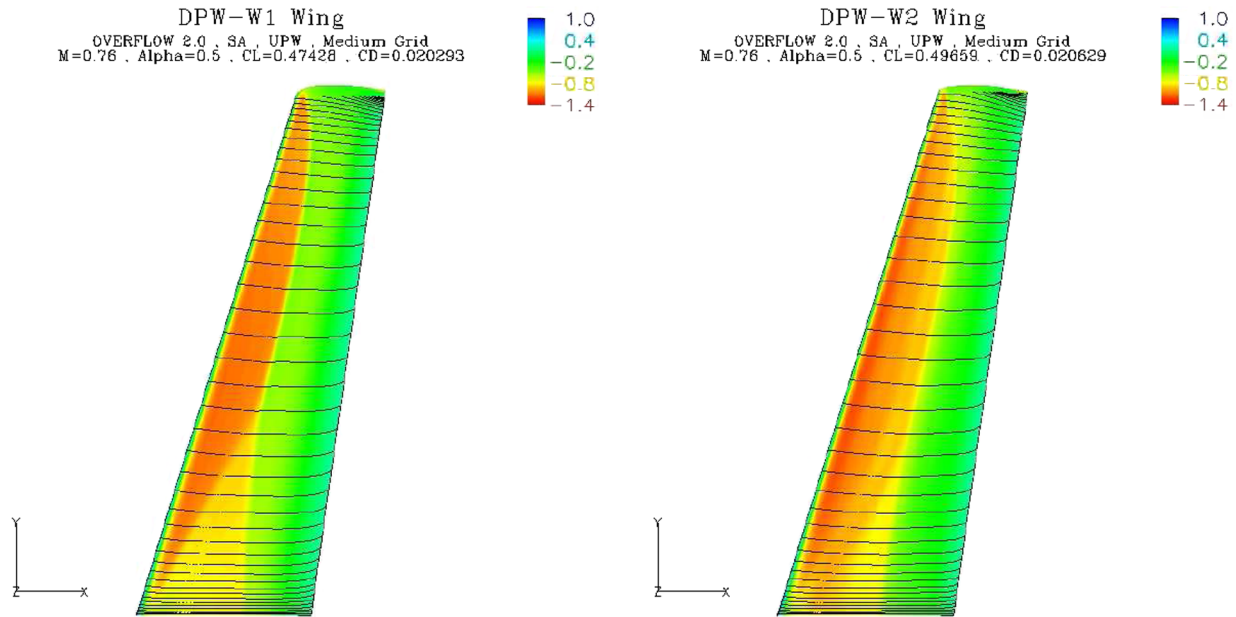
Fig. 47 DPW-W1/W2 surface streamline comparison at $\alpha = 0.5$ deg.
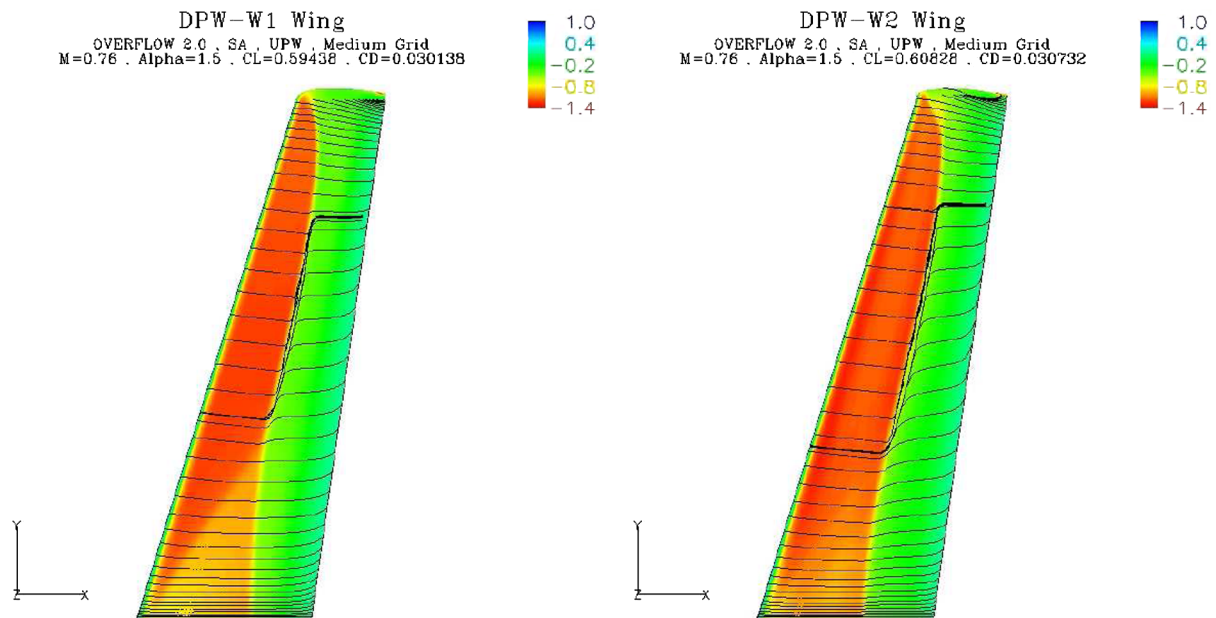
Fig. 48 DPW-W1/W2 surface streamline comparison at $\alpha = 1.5$ deg.

shows that the error in incremental drag associated with a medium-sized grid analysis drops by an order of magnitude when separated flow is not present.

The wing/body and wing-alone medium grids were analyzed at multiple angles of attack to establish drag polars and lift/pitching moment curves. Two turbulence models, the one-equation Spalart–Allmaras and the two-equation Menter SST, were used for some of the DLR-F6 OVERFLOW runs. They yielded similar results with less than 5 counts difference in fixed-C_L drag coefficient and a nearly identical drag polar shape. Comparing the code-to-code results qualitatively, CFL3D exhibited a wavy character in its drag polar, whereas OVERFLOW was smooth. Other than this discrepancy, the angle-of-attack sweep results from the two codes compared well. The following list summarizes areas where CFL3D and OVERFLOW produced similar wing/body results:

1) trends in incremental data (e.g., FX2B had considerably less drag than F6 through the mid-C_L range);

2) the size of the DLR-F6 side-of-body separation bubble and its variation with grid refinement and viscous effects;

3) no DLR-F6 wing trailing-edge separation at 5×10^6 Reynolds number;

4) DLR-F6 wing pressures—namely, shock strength and location on medium and fine grids.

The last three items in this list are based on runs made at the design point C_L of 0.5. The wing-alone results show the two codes compute nearly the same drag for W1 at C_Ls near the design point, but more CFL3D data are needed to comment on incremental trend comparisons for this test case.

Appendix: CFL3D FX2B Data Discrepancy

During the process of writing this paper, a discrepancy was found in the CFL3D FX2B results originally submitted to the workshop: the medium grid data computed for the grid convergence study were
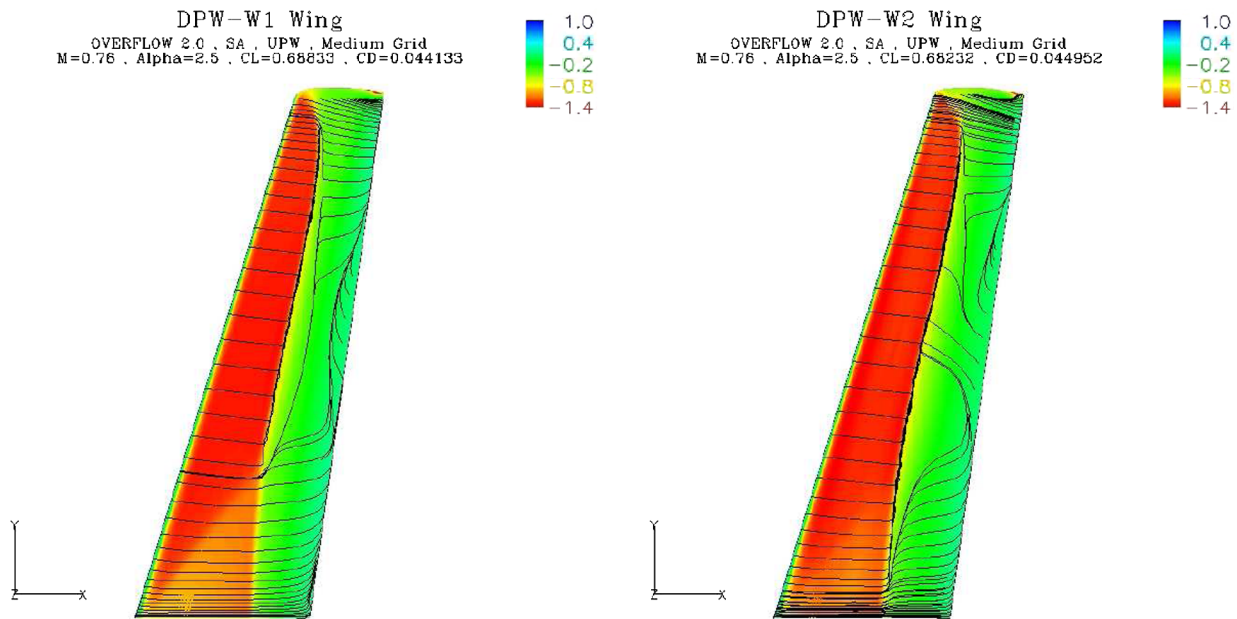
Fig. 49   DPW-W1/W2 surface streamline comparison at $\alpha = 2.5$ deg.

noted to be different than the angle-of-attack sweep data. The angle-of-attack sweep runs were made as a series of restarts using the lower angle-of-attack solutions as a starting point for the next higher angle of attack. Because the grid convergence study required only one data point, those runs were all made from "scratch" (freestream levels). As a troubleshooting exercise, a few of the angle-of-attack sweep runs were subsequently made from scratch and slightly different answers (as much as 3 drag counts) were obtained. The authors were unable to explain this hysteresis type of dependence on initial conditions. All solutions were considered fully converged with residuals dropping several orders of magnitude. Furthermore, the force and moment convergence histories "leveled out" (did not oscillate). This hysteresis behavior did not occur for the F6 case.

Note that although the grids are the same, CFL3D and OVERFLOW did not use the same overset interpolants. Because CFL3D is a cell-centered solver, it could not use the interpolants provided for the node-based OVERFLOW solver; they had to be regenerated. The current method for doing this is an ad hoc process [16]. For the FX2B medium grid, this process yielded nearly 5 times as many orphans than for the F6 grid (which contained 250 orphan points). There were only five orphans in the OVERFLOW grids for both F6 and FX2B. It is possible that issues related to the interpolants/orphans contributed to the discrepancy in FX2B results.

Acknowledgments

The authors acknowledge The Boeing Company and The National Aeronautics and Space Administration for their support in the Drag Prediction Workshop series. We also thank Mark A. DeHaan for his contribution to this work.

References

[1] Hemsch, M. J., "Statistical Analysis of CFD Solutions from the Drag Prediction Workshop," AIAA Paper 2002-0842, Jan. 2002.

[2] Levy, D. W., Vassberg, J. C., Wahls, R. A., Zickuhr, T., Agrawal, S., Pirzadeh, S., and Hemsch, M. J., "Summary of Data from the First AIAA CFD Drag Prediction Workshop," AIAA Paper 2002-0841, Jan. 2002.

[3] 1st AIAA CFD Drag Prediction Workshop, http://aaac.larc.nasa.gov/tsab/cfdlarc/aiaa- dpw/Workshop1/workshop1.html [cited July 2006].

[4] Laflin, K. R., Vassberg, J. C., Wahls, R. A., Morrison, J. H., Brodersen, O., Radowitz, M., Tinoco, E. N., and Godard, J., "Summary of Data from the Second AIAA CFD Drag Prediction Workshop," AIAA Paper 2004-0555, Jan. 2004.

[5] 2nd AIAA CFD Drag Prediction Workshop, http://aaac.larc.nasa.gov/tsab/cfdlarc/aiaa- dpw/Workshop2/workshop2.html [cited July 2006].

[6] Vassberg, J. C., Sclafani, A. J., and DeHaan, M. A., "A Wing-Body Fairing Design for the DLR-F6 Model: A DPW-III Case Study," AIAA Paper 2005-4730, June 2005.

[7] Sclafani, A. J., DeHaan, M. A., and Vassberg, J. C., "OVERFLOW Drag Predictions for the DLR-F6 Transport Configuration: A DPW-II Case Study," AIAA Paper 2004-0393, Jan. 2004.

[8] Brodersen, O., and Sturmer, A., "Drag Prediction of Engine-Airframe Interference Effects Using Unstructured Navier-Stokes Calculations," AIAA Paper 2001-2414, June 2001.

[9] 3rd AIAA CFD Drag Prediction Workshop, http://aaac.larc.nasa.gov/tsab/cfdlarc/aiaa-dpw [cited July 2006].

[10] Vassberg, J. C., DeHaan, M. A., and Sclafani, A. J., "Grid Generation Requirements for Accurate Drag Predictions Based on OVERFLOW Calculations," AIAA Paper 2003-4124, June 2003.

[11] Chan, W. M., Gomez-III, R. J., Rogers, S. E., and Buning, P. G., "Best Practices in Overset Grid Generation," AIAA Paper 2002- 3191, June 2002.

[12] Chan, W. M., Rogers, S. E., Nash, S. M., Buning, P. G., and Meakin, R. L., User's Manual for Chimera Grid Tools, Ver. 1.9. http://people.nas.nasa.gov/wchan/cgt/doc/man.html [cited July 2006].

[13] Chan, W. M., "The OVERGRID Interface for Computational Simulations on Overset Grids," AIAA Paper 2002-3188, June 2002.

[14] Shus, N. E., Dietz, W. E., Nash, S. M., Baker, M. D., and Rogers, S. E., PEGASUS User's Manual, Ver. 5.1c, MICRO CRAFT, July 2000.

[15] Krist, S. L., Biedron, R. T., and Rumsey, C. L., CFL3D User's Manual: Ver. 5.0., NASA NASA-TM 1998-208444, June 1998.

[16] CFL3D Ver. 6.4. http://cfl3d.larc.nasa.gov [cited July 2006].

[17] Menter, F. R., "Two-Equation Eddy-Viscosity Turbulence Models for Engineering Applications," AIAA Journal, Vol. 32, No. 8, 1994, pp. 1598–1605.

[18] Buning, P. G., Jespersen, D. C., Pulliam, T. H., Chan, W. M., Slotnick, J. P., Krist, S. E., and Renze, K. J., OVERFLOW User's Manual, Ver. 1.8l, NASA Langley Research Center, Hampton, VA, 1999.

[19] Spalart, P. R., and Allmaras, S. R., "A One-Equation Turbulence Model for Aerodynamic Flows," La Recherche Aerospatiale, No. 1, 1994, pp. 5–21.

[20] Salas, M. D., "Digital Flight: The Last CFD Aeronautical Grand Challenge," Journal of Scientific Computing, Vol. 28, Nos. 2/3, Sept. 2006, pp. 479–505.
doi:10.1007/s10915-006-9087-7

[21] Mavriplis, D. J., "Grid Resolution Study of a Drag Prediction Workshop Configuration Using the NSU3D Unstructured Mesh Solver," AIAA Paper 2005-4729, June 2005.

[22] Vassberg, J. C., Tinoco, E. N., Mani, M., Brodersen, O. P., Eisfeld, B., Wahls, R. A., Morrison, J. H., Zickuhr, T., Laflin, K. R., and Mavriplis, D. J., "Summary of the Third AIAA CFD Drag Prediction Workshop," AIAA Paper 2007-0260, Jan. 2007.